Received 27 April 2025; revised 1 June 2025; accepted 6 June 2025. Date of publication 10 June 2025; date of current version 27 June 2025.

Digital Object Identifier 10.1109/OJCOMS.2025.3578473

EXIT Chart Analysis of Expectation Propagation-Based Iterative Detection and Decoding

FUGA KOBAYASHI [1] (Graduate Student Member, IEEE), TAKUMI TAKAHASHI [1] (Member, IEEE), SHINSUKE IBI [2] (Senior Member, IEEE), AND HIDEKI OCHIAI [1] (Fellow, IEEE)

[1]Graduate School of Engineering, The University of Osaka, Suita 565-0871, Japan
[2]Faculty of Science and Engineering, Doshisha University, Kyotanabe 610-0394, Japan

CORRESPONDING AUTHOR: T. TAKAHASHI (e-mail: takahashi@comm.eng.osaka-u.ac.jp)

This work was supported in part by the Japan Society for the Promotion of Science (JSPS) KAKENHI under Grant JP23K13335 and Grant JP23K22754; in part by the Japan Science and Technology Agency (JST), CRONOS, Japan, under Grant JPMJCS24N1; and in part by the Ministry of Internal Affairs and Communications (MIC)/FORWARD under Grant JPMI240710001.

ABSTRACT This paper proposes a novel framework for extrinsic information transfer (EXIT) chart analysis to examine the convergence behavior of iterative detection and decoding (IDD) algorithms based on expectation propagation (EP), specifically addressing the extrinsic value exchange mechanism through moment matching (MM). An essential element of IDD algorithm design is the mitigation of self-noise feedback by extrinsic value exchange between the symbol detector and the channel decoder across iterations. This study seeks to compare the extrinsic value exchange mechanisms of established turbo equalization and emerging EP-based IDD, both theoretically and numerically, to elucidate their differences. Turbo equalization utilizes the extrinsic log-likelihood ratio (LLR), whereas EP-based IDD functions in the symbol domain through MM. Extensive simulations of multiple-input multiple-output (MIMO) signal detection indicate that EP-based IDD provides superior bit error rate (BER) performance compared to turbo equalization, especially in demanding scenarios involving higher modulation orders and increased spatial multiplexing loads. To provide theoretical support for these findings, we extend the classical EXIT analysis to include symbol-domain operations. The proposed framework analytically demonstrates that the enhanced detection performance of EP-based IDD arises from the exchange of extrinsic values in the symbol domain, in contrast to conventional turbo equalization, which functions in the LLR domain.

INDEX TERMS Iterative detection and decoding, expectation propagation, moment matching, EXIT chart, MU-MIMO-OFDM systems, high-order modulation.

I. INTRODUCTION

IN THE fifth-generation (5G) advanced and future sixth-generation (6G) networks, the number of wireless devices is expected to increase dramatically due to the advancement of Internet of Things (IoT) technology [1], [2], [3], [4]. In addition to the initially envisioned wireless IoT applications based on low-capacity communications, there is a growing number of use cases requiring high-capacity data uploads from individual devices [5], [6], [7]. There is a pressing need for communication methods that simultaneously satisfy the heterogeneous requirements of enhanced mobile broadband (eMBB) and massive machine-type communications (mMTC) [8], [9]. One of the key technologies to achieve this type of communication is large multi-user multiple-input multiple-output orthogonal frequency-division multiplexing (MU-MIMO-OFDM) [10], [11], [12], where a base station (BS) equipped with a large number of antennas simultaneously provides high-capacity wireless links to multiple user equipment (UE) devices by multiplexing signals across both frequency and spatial domains. In particular, the uplink should play a crucial role as an information infrastructure for collecting massive amounts of data from a large number of UEs [13], [14], [15], [16]. To achieve this, an advanced multi-user detection (MUD) scheme is essential to accurately separate the signals multiplexed in each sub-carrier at the BS receiver [17].

Maximum likelihood detection (MLD) theoretically achieves optimal detection performance. However, due to

its exponential computational complexity with respect to the number of spatially multiplexed streams, MLD becomes impractical for very large MIMO systems [18]. As a result, low-complexity MUD techniques have been widely employed, such as linear minimum mean square error (LMMSE) filters [19]. These detection methods can achieve the performance of MLD when the number of receive (RX) antennas is sufficiently large relative to the number of transmit (TX) streams. Nevertheless, the detection performance progressively deteriorates as the number of TX streams increases in relation to RX antennas [20]. This can result in significant performance degradations, particularly when a massive number of devices are simultaneously connected [21].

IDD has been investigated as a technique capable of achieving detection performance close to that of MLD with polynomial computational complexity, even in spatially densely loaded MIMO settings [22], [23]. By exchanging *extrinsic* information between the symbol detector and the channel decoder at the receiver side, detection accuracy can be gradually improved, assuming the presence of channel coding at the transmitter side. The most well-known IDD algorithm is soft canceller followed by the minimum mean square error (SC/MMSE) turbo equalization [24], [25], [26]. It iteratively exchanges the LLR between the LMMSE detector with parallel interference cancellation and the channel decoder. This *turbo principle* enables the resulting detector to achieve near-optimal performance [27], [28]. Specifically, assuming that the consistency condition [29], [30] of LLRs is satisfied, extrinsic LLRs fed back to the detector are generated by subtracting the detector output (decoder input) LLRs from the decoder output LLRs, thus enabling extrinsic information transfer without self-noise feedback [31], [32].

Another method of IDD construction that has garnered interest in recent years is extrinsic information exchange based on EP [33], [34], [35], [36]. This method generates symbol replicas (soft estimates) from the posterior LLR of the decoder output based on the conditional expectation and then decouples the symbol information of the detector output through MM to facilitate extrinsic information exchange [37], [38]. A key difference between these two IDDs is that the EP-based IDD generates extrinsic values in the symbol domain by taking into account the discrete configurations of the constellation points, whereas turbo equalization directly generates extrinsic values in the LLR domain. An IDD algorithm construction based on EP was initially introduced in [37], where numerical results indicated its superior performance compared to SC/MMSE turbo equalization. In [37], the EP-based iterative detector is integrated into IDD as an inner loop structure, primarily aimed at assessing the impact of advanced iterative detection on the enhancement of overall IDD performance. To our knowledge, no previous work sufficiently compares and validates these two IDD design methodologies with an emphasis on extrinsic value generation. There has also been inadequate investigation of the convergence behavior of EP-based IDD utilizing extrinsic value generation through MM.

An EXIT chart is often used to analyze the iterative convergence behavior of IDD [39], [40], [41], [42], [43], [44]. This method characterizes the information exchange between two modules, specifically the detector and decoder, as a transfer of mutual information (MI) [39]. This facilitates a quantitative and visual assessment of the enhancement of information regarding the unknown signal across each module, thereby enabling a semi-theoretical analysis of the convergence behavior of IDD. The iterative behavior of SC/MMSE turbo equalization has been thoroughly examined through the EXIT chart in a significant body of literature [45], [46], [47]. However, previous work has not examined EP-based IDD through the EXIT chart to elucidate its iterative convergence characteristics, particularly in systems employing higher-order modulation schemes. This is mainly due to the necessity of complex mathematical manipulations to represent the exchange of extrinsic values through MM in the symbol domain as an exchange of MI. Higher-order modulation schemes, such as 16 quadrature amplitude modulation (QAM) or greater, require non-orthogonal bit-to-symbol mappings that involve information-theoretically non-invertible operations for generating symbol estimates from bit-wise LLRs. Thus, incorporating extrinsic value generation through MM in the symbol domain complicates the MI calculation. Moreover, the use of symbol estimates as inputs for plotting the EXIT curves, instead of LLRs, precludes the application of consistent modeling previously established for LLRs, thereby complicating the implementation of EXIT chart analysis for EP-based IDD.

Building on the above discussions, this paper first conducts extensive simulations of large MU-MIMO-OFDM signal detection to compare the BER performance of SC/MMSE turbo equalization, which exchanges extrinsic values in the LLR domain, with EP-based IDD, which exchanges extrinsic values in the symbol domain through MM. The comparative results indicate performance differences due to the distinct mechanisms of extrinsic value generation across different system configurations. To semi-analytically support these findings, we further introduce a new EXIT chart analysis framework that extends classical EXIT chart analysis to accommodate symbol-domain extrinsic value generation through MM. This framework enables the analysis of the convergence behavior of EP-based IDD.

The contributions of this paper are summarized as follows:

- We design an EP-based IDD by replacing the extrinsic value exchange mechanism of SC/MMSE turbo equalization with MM, and comprehensively compare its performance through large MU-MIMO-OFDM signal detection simulations. The BER performance of EP-based IDD demonstrates a marked improvement over conventional SC/MMSE turbo equalization, especially in challenging scenarios involving higher modulation orders and increased spatial multiplexing loads. This

enhancement occurs due to the difficulties faced by turbo equalization in sustaining the consistency condition of LLRs under challenging conditions, which obstructs the effective exchange of extrinsic values across iterations. In contrast, EP-based IDD utilizes symbol-domain MM to align with the second-order moment (*i.e.*, expectation and variance), effectively accounting for the discrete nature of the constellation points and facilitating a more robust and reliable exchange of extrinsic values.

- We design an EXIT chart to analyze the extrinsic value exchange through MM in EP-based IDD and visualize the effects of discrete symbol constraints. In EP-based IDD, the two modules exchange information in the form of symbol estimates. This requires the accurate modeling of input and output MI derived from these symbols when generating the EXIT curves for each module. Furthermore, when a non-orthogonal bit-to-symbol mapping rule is used, the generation process of symbol estimates from bit-wise LLRs induces information loss. To address this, a mechanism is introduced to remeasure MI following symbol generation, facilitating the accurate plotting of EXIT curves. Our analysis reveals that the tunnel between the detector and decoder EXIT curves for EP-based IDD is wider compared to that of conventional SC/MMSE turbo equalization, indicating that extrinsic value generation through MM can yield enhanced performance improvements in more challenging conditions by leveraging the discrete nature of the symbols. The observed consistency between the EXIT trajectories and the EXIT curves quantitatively validates the proposed analytical framework and offers new insights into the design of IDD algorithms for practical system sizes.

To the best of our knowledge, this is the first study that systematically evaluates EP-based IDD in terms of its extrinsic value generation mechanism and compares it to the conventional one via extrinsic LLRs in SC/MMSE turbo equalization. We develop an EXIT chart analysis that allows for quantitative examination of extrinsic value exchange using MM. This framework offers new insights into IDD design, particularly with respect to convergence behavior, which constitutes another significant contribution.

A. RELATED WORK AND OUR CONTRIBUTIONS

The double EP (DEP) algorithm, proposed in [37], [38], is the most widely studied EP-based IDD algorithm. It has two loops: an inner loop that performs iterative detection using the message passing algorithm (MPA) without a decoder and an outer loop that carries out IDD. Both the inner and outer loops involve extrinsic value exchange through MM. This is, to our knowledge, the inaugural literature to explicitly include EP into IDD design. Numerical studies indicated that DEP significantly outperforms SC/MMSE turbo equalization in detection performance, primarily by enhancing the capabilities of the signal detector through the substitution of linear MMSE with EP-based MPA. The method for generating extrinsic value was little addressed. These findings prompted our investigation, which seeks to ascertain the most effective IDD design for extrinsic value exchange. In fact, the EP-based IDD presented in this paper is consistent with the special case of DEP where the number of iterations of the inner loop is set to 1. To date, no study has systematically compared and validated the two IDD design methods–EP-based IDD and SC/MMSE turbo equalization–under various system configurations using exactly the same detector and decoder.

In a related work on EXIT chart analysis, a cascade connection scheme between EP-based MPA and SC/MMSE turbo equalization was proposed in [48], and its convergence behavior was analyzed using the EXIT chart. This study, which builds upon the earlier cascade connection scheme of probabilistic data association (PDA) [49], [50] and SC/MMSE turbo equalization proposed in [51], demonstrates that replacing PDA with EP in the former stage enables higher detection accuracy, particularly for overload MIMO signal detection. The EXIT chart analysis examines the convergence behavior within the subsequent IDD loop during the later stage. The results indicate that employing EP as the MPA in the earlier stage enhances the overall convergence characteristics. In [48], the IDD loop utilizes conventional turbo equalization, incorporating extrinsic value exchange through extrinsic LLRs. However, the analysis of EP-based IDD using MM remains unaddressed.

Another important related work in the analysis of the iterative behavior of EP-based IDD is the convergence analysis of extrinsic-massage-aided orthogonal approximate message passing (EMA-OAMP) [52], which extends OAMP [53] to coded systems. Although there are some structural differences between EMA-OAMP and our EP-based IDD, these algorithms coincide in the large-system limit.[1] Therefore, the state evolution (SE) framework provided in [52], with appropriate consideration of the adopted nonlinear detector (*i.e., denoiser*), can be applied to analyze the asymptotic behavior of EP-based IDD under the large-system limit [36]. However, while SE is a powerful and well-established tool for analyzing convergence in asymptotic regimes, it is applicable only when all exchanged messages can be accurately approximated as Gaussian [54], [55], [56], which requires extremely large system dimensions–typically on the order of hundreds or more. SE tracks the evolution of message variance across iterations but cannot account for finite-size effects or deviations from Gaussianity in decoder outputs [57], [58], [59], [60]. Indeed, even with a MIMO configuration of $(N, M) = (64, 64)$–larger than the systems considered in this paper–noticeable discrepancies between SE predictions and simulation results have been reported in [52]. Thus, while SE is valuable for theoretical

[1]This corresponds to the idealized system, in which the input and output dimensions, M and N, of the linear system are infinite for a given compression ratio $\xi \triangleq \frac{N}{M}$.

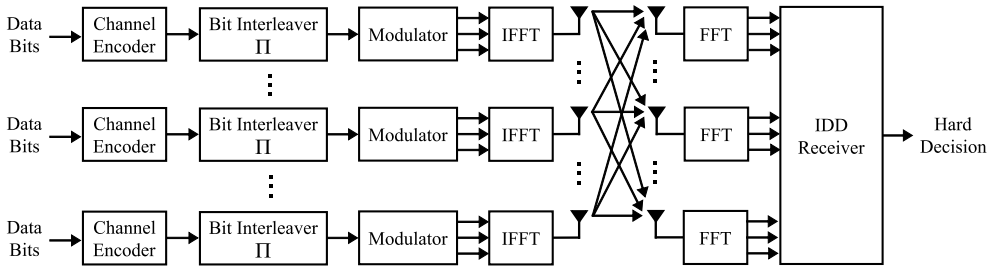

FIGURE 1. MU-MIMO-OFDM system block diagram, including the IDD receiver block.

asymptotic analysis, it is insufficient for precisely defining the convergence behavior of IDD algorithms under actual system sizes.

In contrast, our proposed framework for EP-based IDD does not rely on simple Gaussian approximations. Instead, the messages (*i.e.,* extrinsic values) exchanged between the two modules are carefully modeled based on the specific operations within each module and the actual statistical properties across the iteration process. This approach allows for highly accurate analysis of iterative behavior in realistic finite-sized systems, complementing SE by providing robust insights where SE is challenging to apply.

Finally, as a recent advancement in related IDD algorithm designs, EP-based IDD structures employing polar codes as error correction codes have been proposed [61], [62], aiming to reduce computational complexity and enhance performance by leveraging the code structure. Although various modified designs have been introduced, as long as extrinsic value exchange is performed through MM based on EP, the analytical framework proposed in this study remains applicable. Our proposed framework thus offers a cohesive and widely applicable method for the analysis of EP-based IDD structures, accommodating the ongoing evolution of IDD designs to satisfy emerging system requirements.

B. MATHEMATICAL NOTATIONS

Sets of real and complex numbers are denoted by $\mathbb{R}$ and $\mathbb{C}$, respectively. Vectors and matrices are denoted in lower- and upper-case bold-face letters. The transpose and conjugate transpose operators are denoted by $(\cdot)^{\mathsf{T}}$ and $(\cdot)^{\mathsf{H}}$, respectively. The imaginary unit is denoted by $\mathrm{j} \triangleq \sqrt{-1}$. The real and imaginary parts of a complex quantity are denoted by $\Re[\,\cdot\,]$ and $\Im[\,\cdot\,]$, respectively. For any countable finite set $\mathcal{A}$, let $|\mathcal{A}|$ denote the number of elements in $\mathcal{A}$. The $a \times a$ identity matrix is denoted by $\boldsymbol{I}_a$. The complex Gaussian distribution with a mean a and a variance b is denoted by $\mathcal{CN}(a, b)$. The probability mass function (PMF) and probability density function (PDF) with respect to random variable a are denoted by $P_{\mathsf{a}}[\,\cdot\,]$ and $p_{\mathsf{a}}(\cdot)$, respectively. Also, the conditional PMF and PDF with respect to a given the realized value b' of the random value b are denoted by $P_{\mathsf{a}|\mathsf{b}}[\,\cdot\,|b']$ and $p_{\mathsf{a}|\mathsf{b}}(\cdot|b')$, respectively. The expected value of a random variable is denoted by $\mathbb{E}[\,\cdot\,]$. For brevity, the abbreviated notation $\sum_{i\neq j}^{I} a_i \triangleq \sum_{i=1}^{I} a_i - a_j$ is used.

II. SYSTEM MODEL

Consider an uplink massive MU-MIMO-OFDM system composed of a BS having N antennas and serving M synchronized single-antenna UE devices. Each of M UEs performs spatial multiplexing transmission to a BS receiver as shown in Fig. 1. At the m-th UE, the data bits $\boldsymbol{b}_m \triangleq [b_{m,1}, \ldots, b_{m,n_{\mathrm{b}}}, \ldots b_{m,N_{\mathrm{b}}}] \in \{0,1\}^{1\times N_{\mathrm{b}}}$ are encoded to the code bits $\boldsymbol{c}_m \triangleq [c_{m,1}, \ldots, c_{m,n_{\mathrm{c}}}, \ldots, c_{m,N_{\mathrm{c}}}] \in \{0,1\}^{1\times N_{\mathrm{c}}}$, with the code length N_{c} and the code rate $r_{\mathrm{c}} \triangleq N_{\mathrm{b}}/N_{\mathrm{c}}$. After the interleaver processing Π, the code bits are then modulated to the frequency-domain symbols $\boldsymbol{x}_m^{\rightarrow} \triangleq [x_{m,1}, \ldots, x_{m,k}, \ldots, x_{m,K}] \in \mathbb{C}^{1\times K}$, where each symbol is selected from the set of QAM symbol candidate points $\mathcal{X}$ with $Q \triangleq |\mathcal{X}|$ denoting the modulation order. The symbol length is $K \triangleq N_{\mathrm{c}}/\log_2 Q$, and the average power density of the modulated symbol is E_{s}. Each UE maps the symbol stream $\boldsymbol{x}_m^{\rightarrow}$ to a time-frequency resource using inverse fast Fourier transform (IFFT), and then transmits the resulting signal using OFDM. In the following, we assume that M UEs perform spatial multiplexing transmission over time-frequency resources consisting of R OFDM symbols (time) $\times$ L subcarriers (frequency). During the transmission of R OFDM symbols, the wireless channel is assumed to be constant, but it varies for each subcarrier depending on frequency selectivity. The insertion and removal of cyclic prefix in OFDM transmission are assumed to be carried out ideally, and the receiver performs MUD on the received frequency-domain MIMO signal.

Without loss of generality, consider the spatial multiplexing transmission of the k-th modulated symbol vector $\boldsymbol{x}_k[\ell] \triangleq [x_{1,k}[\ell], \ldots, x_{m,k}[\ell], \ldots, x_{M,k}[\ell]]^{\mathsf{T}} \in \mathbb{C}^{M\times 1}$ using the ℓ-th subcarrier. However, the relationship between the indices ℓ and k is determined by the mapping rule of the modulated symbols to the time-frequency resources, and the IDD process is performed independently of ℓ, so the qualifier $[\ell]$ is omitted hereafter. The corresponding frequency-domain RX symbol vector can be expressed as

$$\boldsymbol{y}_k \triangleq \left[y_{1,k}, \ldots, y_{n,k}, \ldots, y_{N,k}\right]^{\mathsf{T}} = \boldsymbol{H}_k \boldsymbol{x}_k + \boldsymbol{z}_k, \tag{1}$$

where $\boldsymbol{H}_k \triangleq [\boldsymbol{h}_{1,k}, \ldots, \boldsymbol{h}_{m,k}, \ldots, \boldsymbol{h}_{M,k}] \in \mathbb{C}^{N\times M}$ is the corresponding frequency-domain MIMO channel matrix, and $\boldsymbol{h}_{m,k} \in \mathbb{C}^{N\times 1}$ denotes the m-th column vector of $\boldsymbol{H}_k$. In addition, $\boldsymbol{z}_k \triangleq [z_{1,k}, \ldots, z_{n,k}, \ldots, z_{N,k}]^{\mathsf{T}} \in \mathbb{C}^{N\times 1}$ is the corresponding additive white Gaussian noise (AWGN)

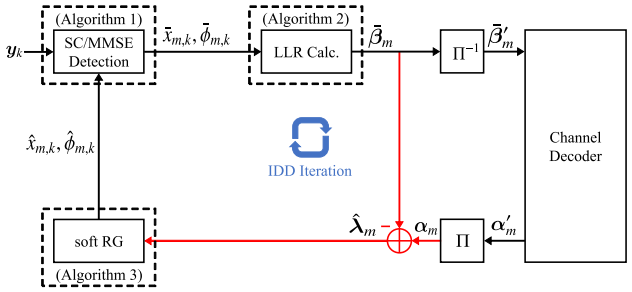

(a) SC/MMSE turbo equalization.

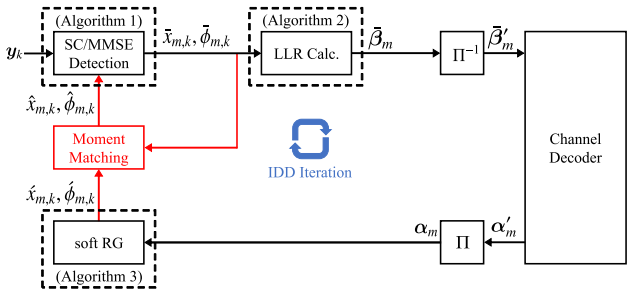

(b) EP-based IDD.

FIGURE 2. Block diagram of two IDD receiver configurations.

vector, each entry of which follows $\mathcal{CN}(0, N_0)$ with N_0 denoting the noise power density.

At the receiver, IDD is performed to estimate the information bits by iteratively exchanging information between the signal detector, which estimates the TX vectors $\boldsymbol{x}_k, \forall k$, based on the knowledge of $\boldsymbol{y}_k, \forall k$, and $\boldsymbol{H}_k, \forall k$, in (1), and the channel decoder, which performs error corrections.

For simplicity, we assume that the channel matrix $\boldsymbol{H}_k, \forall k$, is estimated without error at the BS receiver.

III. RECEIVER DESIGN BASED ON IDD

Fig. 2 shows the block diagram of two IDD receiver configurations, (a) SC/MMSE turbo equalization and (b) EP-based IDD.[2] As can be seen by comparing the two diagrams, the modules that constitute the two IDDs are identical, and only the wiring structure between the modules highlighted in red differs due to differences in the extrinsic value exchange mechanism. Thus, these two can be compared to verify the change in performance due to different extrinsic value exchange mechanisms.

In this section, we first describe each of the modules that constitute IDD in turn, including the extrinsic value exchange mechanism via extrinsic LLRs, according to the block diagram of SC/MMSE turbo equalization shown in Fig. 2(a). Next, we describe the extrinsic value exchange mechanism via MM in EP-based IDD shown in Fig. 2(b). Finally, we summarize the algorithm structure of the two IDD receivers using pseudocode and compare the BER performance by computer simulation.

[2]The receiver configuration used in this paper does not perform self-iterative detection (SID) that performs iterative processing without the channel decoder. Note that it is different from DEP [37], which consists of an inner loop that performs the EP-based SID and an outer loop that performs IDD with the channel decoder.

A. SC/MMSE DETECTOR

First, we describe the SC/MMSE detector, focusing on the detection of the TX symbol $x_{m,k}$ from the RX vector $\boldsymbol{y}_k$ and the channel matrix $\boldsymbol{H}_k$ based on (1).

For later convenience, let us define the *soft replica* (*i.e.*, tentative estimate) of $x_{m,k}$ as $\hat{x}_{m,k}$, such that its mean square error (MSE) can be expressed as

$$\hat{\phi}_{m,k} \triangleq \mathbb{E}\Big[\big|x_{m,k} - \hat{x}_{m,k}\big|^2\Big]. \tag{2}$$

At the first iteration ($t = 1$), the soft replica and its MSE are appropriately initialized, *i.e.*, $\hat{x}_{m,k} = \mathbb{E}[x_{m,k}] = 0$ and $\hat{\phi}_{m,k} = \mathbb{E}[|x_{m,k}|^2] = E_{\mathrm{s}}$. The soft replica generation in the second and subsequent iterations will be explained later.

Let us start with the soft interference cancellation (soft IC) for the RX vector $\boldsymbol{y}_k$ with the aid of the soft replicas $\hat{x}_{m,k}, \forall m$ generated in the previous iteration. In the detection of $x_{m,k}$, the cancellation process is expressed as

$$\begin{aligned}\tilde{\boldsymbol{y}}_{m,k} &= \boldsymbol{y}_k - \underbrace{\sum_{i\neq m}^{M} \boldsymbol{h}_{i,k}\hat{x}_{i,k}}_{\text{Inter-symbol interference cancellation}} \\ &= \boldsymbol{h}_{m,k}x_{m,k} + \underbrace{\sum_{i\neq m}^{M} \boldsymbol{h}_{i,k}\big(x_{i,k} - \hat{x}_{i,k}\big) + \boldsymbol{z}_k}_{\triangleq \boldsymbol{v}_{m,k}\text{: Residual interference plus noise}}. \end{aligned} \tag{3}$$

Under large-system conditions, the residual interference-plus-noise component of (3) can be approximated as a multivariate complex Gaussian random vector in conformity with central limit theorem (CLT). This approximation is referred to as vector Gaussian approximation (VGA) [18].

Accordingly, the conditional PDF of (3), given $x_{m,k}$, can be expressed as

$$\begin{aligned} &p_{\tilde{\mathbf{y}}_{m,k}|\mathsf{x}_{m,k}}\big(\tilde{\boldsymbol{y}}_{m,k}|x_{m,k}\big) \\ &\propto \exp\Big[-\big(\tilde{\boldsymbol{y}}_{m,k} - \boldsymbol{h}_{m,k}x_{m,k}\big)^{\mathsf{H}}\boldsymbol{\Xi}_{m,k}^{-1}\big(\tilde{\boldsymbol{y}}_{m,k} - \boldsymbol{h}_{m,k}x_{m,k}\big)\Big], \end{aligned} \tag{4}$$

where

$$\boldsymbol{\Xi}_{m,k} \triangleq \mathbb{E}\Big[\boldsymbol{v}_{m,k}\boldsymbol{v}_{m,k}^{\mathsf{H}}\Big] = \boldsymbol{\Xi}_k - \hat{\phi}_{m,k}\boldsymbol{h}_{m,k}\boldsymbol{h}_{m,k}^{\mathsf{H}}, \tag{5}$$

with

$$\boldsymbol{\Xi}_k \triangleq \sum_{m=1}^{M} \hat{\phi}_{m,k}\boldsymbol{h}_{m,k}\boldsymbol{h}_{m,k}^{\mathsf{H}} + N_0\boldsymbol{I}_N. \tag{6}$$

Using $\boldsymbol{\Xi}_k$, the conditional PDF of (4) can be written as

$$p_{\tilde{\mathbf{y}}_{m,k}|\mathsf{x}_{m,k}}\big(\tilde{\boldsymbol{y}}_{m,k}|x_{m,k}\big) \propto \exp\left[-\frac{\big|x_{m,k} - \bar{x}_{m,k}\big|^2}{\bar{\phi}_{m,k}}\right], \tag{7}$$

with

$$\bar{x}_{m,k} = \frac{1}{\eta_{m,k}}\boldsymbol{h}_{m,k}^{\mathsf{H}}\boldsymbol{\Xi}_k^{-1}\tilde{\boldsymbol{y}}_{m,k}, \quad \bar{\phi}_{m,k} = \frac{1 - \eta_{m,k}\hat{\phi}_{m,k}}{\eta_{m,k}}, \tag{8}$$

Algorithm 1 SC/MMSE Detector

Require: $\boldsymbol{y}_k, \boldsymbol{H}_k, \{\hat{x}_{m,k}, \hat{\phi}_{m,k}, \forall m\}$
Ensure: $\{\bar{x}_{m,k}, \bar{\phi}_{m,k}, \forall m\}$

1: $\forall m$:$\tilde{\boldsymbol{y}}_{m,k} = \boldsymbol{y}_k - \sum_{i\neq m}^{M} \boldsymbol{h}_{i,k}\hat{x}_{i,k}$
2: $\forall m$:$\boldsymbol{\Xi}_k^{-1} = \left(\sum_{m=1}^{M} \hat{\phi}_{m,k}\boldsymbol{h}_{m,k}\boldsymbol{h}_{m,k}^{\mathsf{H}} + N_0\boldsymbol{I}_N\right)^{-1}$
3: $\forall m$:$\eta_{m,k} = \boldsymbol{h}_{m,k}^{\mathsf{H}}\boldsymbol{\Xi}_k^{-1}\boldsymbol{h}_{m,k}$
4: $\forall m$:$\bar{x}_{m,k} = \frac{1}{\eta_{m,k}}\boldsymbol{h}_{m,k}^{\mathsf{H}}\boldsymbol{\Xi}_k^{-1}\tilde{\boldsymbol{y}}_{m,k}$
5: $\forall m$:$\bar{\phi}_{m,k} = \frac{1-\eta_{m,k}\hat{\phi}_{m,k}}{\eta_{m,k}}$

where $\eta_{m,k} = \boldsymbol{h}_{m,k}^{\mathsf{H}}\boldsymbol{\Xi}_k^{-1}\boldsymbol{h}_{m,k}$, which is derived by applying the matrix inversion lemma to eliminate the dependency of $\boldsymbol{\Xi}_{m,k}$ in (5) on the user index m, allowing us to share the same inverse matrix $\boldsymbol{\Xi}_k^{-1}$ for $\forall m$ [50].

For later convenience, the pseudocode of the SC/MMSE signal detection algorithm is given in Alg. 1.

B. LLR CALCULATOR

Next, the bit-wise LLRs are calculated based on the output of SC/MMSE detector in (8). When $x_{m,k}$ consists of $S \triangleq \log_2 Q$ coded bits $c_{1,m,k}, \ldots, c_{s,m,k}, \ldots, c_{S,m,k}$, the bit-wise LLR corresponding to $c_{s,m,k}$ can be expressed as

$$\bar{\beta}\left(c_{s,m,k}\right) \triangleq \ln\left(\frac{\sum_{x\in\mathcal{X}|c_s=1} p_{\bar{\mathsf{x}}_{m,k}|\mathsf{x}_{m,k}}\left(\bar{x}_{m,k}|x\right)}{\sum_{x\in\mathcal{X}|c_s=0} p_{\bar{\mathsf{x}}_{m,k}|\mathsf{x}_{m,k}}\left(\bar{x}_{m,k}|x\right)}\right), \tag{9}$$

with

$$p_{\bar{\mathsf{x}}_{m,k}|\mathsf{x}_{m,k}}\left(\bar{x}_{m,k}|x\right) \propto \exp\left[-\frac{\left|\bar{x}_{m,k}-x\right|^2}{\bar{\phi}_{m,k}}\right], \tag{10}$$

where $\mathcal{X}|c_s = c$ $(c \in \{0,1\})$ denotes a set of candidate symbol points such that the s-th bit c_s constituting x is c.

As an example, when the modulation scheme is Gray-coded quadrature phase-shift keying (QPSK), *i.e.*, $\mathcal{X} \triangleq \{\pm\sqrt{E_s/2} \pm \mathrm{j}\sqrt{E_s/2}\}$, $Q = 4$, $S = 2$, the bit-wise LLR in (9) can be rewritten as

$$\bar{\beta}\left(c_{1,m,k}\right) = \frac{2\sqrt{2E_s}}{\bar{\phi}_{m,k}}\Re\left[\bar{x}_{m,k}\right], \tag{11a}$$

$$\bar{\beta}\left(c_{2,m,k}\right) = \frac{2\sqrt{2E_s}}{\bar{\phi}_{m,k}}\Im\left[\bar{x}_{m,k}\right]. \tag{11b}$$

The pseudocode of the LLR calculator generalized to any modulation scheme is given in Alg. 2.

C. EXTRINSIC VALUE EXCHANGE VIA EXTRINSIC LLRS

As shown in Fig. 2(a), in SC/MMSE turbo equalization, the detector output LLR $\bar{\boldsymbol{\beta}}_m$ is first de-interleaved to generate the decoder input LLR $\bar{\boldsymbol{\beta}}_m'$ and then input to the decoder. The decoder output LLR $\boldsymbol{\alpha}_m'$ is then interleaved to generate the posterior LLR $\boldsymbol{\alpha}_m$, and the posterior LLR is subtracted from the prior LLR to generate the extrinsic LLR $\hat{\boldsymbol{\lambda}}_m$.

Algorithm 2 LLR Calculator (LLR Calc.)

Require: $\left\{\bar{x}_{m,k}, \bar{\phi}_{m,k}, \forall k\right\}$
Ensure: $\bar{\boldsymbol{\beta}}_m \triangleq [\bar{\beta}_{m,1}, \cdots, \bar{\beta}_{m,n_c}, \cdots, \bar{\beta}_{m,N_c}] \in \mathbb{R}^{1\times N_c}$

1: $\forall k, x$:$q_{m,k}(x) = \exp\left[-\frac{\left|\bar{x}_{m,k}-x\right|^2}{\bar{\phi}_{m,k}}\right]$
2: $\forall s, k$: $\bar{\beta}(c_{s,m,k}) \triangleq \ln\left(\frac{\sum_{x\in\mathcal{X}|c_s=1} q_{m,k}(x)}{\sum_{x\in\mathcal{X}|c_s=0} q_{m,k}(x)}\right)$
3: $\forall k$: $\bar{\boldsymbol{\beta}}_{m,k} = [\bar{\beta}(c_{1,m,k}), \ldots, \bar{\beta}(c_{s,m,k}), \ldots, \bar{\beta}(c_{S,m,k})]$
4: $\bar{\boldsymbol{\beta}}_m = [\bar{\boldsymbol{\beta}}_{m,1}, \ldots, \bar{\boldsymbol{\beta}}_{m,k}, \ldots, \bar{\boldsymbol{\beta}}_{m,K}]$

Assume that the detector output LLR $\bar{\boldsymbol{\beta}}_m$ is obtained for the m-th UE. First, $\bar{\boldsymbol{\beta}}_m$ is de-interleaved to generate the decoder input LLR as

$$\bar{\boldsymbol{\beta}}_m' = \Pi^{-1}\left(\bar{\boldsymbol{\beta}}_m\right), \tag{12}$$

where $\Pi(\cdot)$ is the interleaver operation used at the transmitter, and $\Pi^{-1}(\cdot)$ is the reverse operation (*i.e.*, de-interleaver operation). The obtained LLR $\bar{\boldsymbol{\beta}}_m'$ is then input to a soft-decision decoder, and after appropriate error correction processing, the decoder output LLR $\boldsymbol{\alpha}_m'$ is obtained. After applying the interleaver operation again, the posterior LLR is obtained as

$$\boldsymbol{\alpha}_m \triangleq \left[\alpha_{m,1}, \ldots, \alpha_{m,n_c}, \ldots, \alpha_{m,N_c}\right] = \Pi\left(\boldsymbol{\alpha}_m'\right), \tag{13}$$

Finally, the extrinsic LLR is generated by subtracting the prior LLR $\bar{\boldsymbol{\beta}}_m$ from the posterior LLR $\boldsymbol{\alpha}_m$ based on the turbo principle as

$$\hat{\boldsymbol{\lambda}}_m \triangleq \left[\hat{\lambda}_{m,1}, \ldots, \hat{\lambda}_{m,n_c}, \ldots, \hat{\lambda}_{m,N_c}\right] = \boldsymbol{\alpha}_m - \bar{\boldsymbol{\beta}}_m. \tag{14}$$

D. SOFT REPLICA GENERATOR

Let us define the bit vector comprising the TX symbol $x_{m,k}$ as $\boldsymbol{c}_{m,k} \triangleq [c_{1,m,k}, \ldots, c_{s,m,k}, \ldots, c_{S,m,k}] \in \{0,1\}^{1\times S}$ and the corresponding extrinsic LLR vector as $\hat{\boldsymbol{\lambda}}_{m,k} \triangleq [\hat{\lambda}(c_{1,m,k}), \ldots, \hat{\lambda}(c_{s,m,k}), \ldots, \hat{\lambda}(c_{S,m,k})] \in \mathbb{R}^{1\times S}$. Note that $\hat{\boldsymbol{\lambda}}_m = [\hat{\boldsymbol{\lambda}}_{m,1}, \ldots, \hat{\boldsymbol{\lambda}}_{m,k}, \ldots, \hat{\boldsymbol{\lambda}}_{m,K}]$. The soft replica of $x_{m,k}$ and its MSE can be obtained in general from the conditional expectation given $\hat{\boldsymbol{\lambda}}_{m,k}$, as

$$\hat{x}_{m,k} = \sum_{x\in\mathcal{X}} xP_{\mathsf{x}_{m,k}|\hat{\boldsymbol{\lambda}}_{m,k}}\left[x|\hat{\boldsymbol{\lambda}}_{m,k}\right], \tag{15a}$$

$$\hat{\phi}_{m,k} = \sum_{x\in\mathcal{X}} \left|x-\hat{x}_{m,k}\right|^2 P_{\mathsf{x}_{m,k}|\hat{\boldsymbol{\lambda}}_{m,k}}\left[x|\hat{\boldsymbol{\lambda}}_{m,k}\right]. \tag{15b}$$

Assuming the independence among the bit-wise LLRs on the premise of interleaving process, we have [63], [64]

$$P_{\mathsf{x}_{m,k}|\hat{\boldsymbol{\lambda}}_{m,k}}\left[x|\hat{\boldsymbol{\lambda}}_{m,k}\right] = \prod_{s=1}^{S} P_{\mathsf{c}_{s,m,k}|\hat{\lambda}(c_{s,m,k})}\left[c_s|\hat{\lambda}\left(c_{s,m,k}\right)\right]. \tag{16}$$

Algorithm 3 Soft Replica Generator (Soft RG)

Require: $\hat{\boldsymbol{\lambda}}_m = \left[\hat{\boldsymbol{\lambda}}_{m,1}, \ldots, \hat{\boldsymbol{\lambda}}_{m,k}, \ldots, \hat{\boldsymbol{\lambda}}_{m,K}\right] \in \mathbb{R}^{1\times N_c}$
Ensure: $\{\hat{x}_{m,k}, \hat{\phi}_{m,k}, \forall k\}$

1: $\forall s, k, x{:}u(c_{s,m,k}, x)$
2: $= \frac{1}{2^S}\prod_{s=1}^{S}\left(1 + (2c_s - 1)\tanh\left[\frac{\hat{\lambda}(c_{s,m,k})}{2}\right]\right)$
3: $\forall k{:}\hat{x}_{m,k} = \sum_{x\in\mathcal{X}} x \cdot u(c_{s,m,k}, x)$
4: $\forall k{:}\hat{\phi}_{m,k} = \sum_{x\in\mathcal{X}} |x|^2 \cdot u(c_{s,m,k}, x) - |\hat{x}_{m,k}|^2$

In addition, when the bit-wise LLRs have ideal statistical properties that meet the consistency condition [30],[3] the bit-wise conditional probability in (16) can be expressed as

$$P_{\mathsf{c}_{s,m,k}|\hat{\lambda}(c_{s,m,k})}\left[c_s|\hat{\lambda}(c_{s,m,k})\right] = \frac{1}{2}\left(1 + (2c_s - 1)\tanh\left[\frac{\hat{\lambda}(c_{s,m,k})}{2}\right]\right), \quad (17)$$

As an example, when the modulation scheme is Gray-coded QPSK, from (16) and (17), the soft replica and its MSE in (15) can be rewritten as [57]

$$\hat{x}_{m,k} = \sqrt{\frac{E_s}{2}}\left(\tanh\left[\frac{\hat{\lambda}(c_{1,m,k})}{2}\right] + \mathrm{j}\tanh\left[\frac{\hat{\lambda}(c_{2,m,k})}{2}\right]\right), \quad (18a)$$

$$\hat{\phi}_{m,k} = E_s - \left|\hat{x}_{m,k}\right|^2. \quad (18b)$$

The pseudocode of the LLR calculator for a general modulation scheme is given in Alg. 3.

The one iteration of SC/MMSE turbo equalization is completed by feeding back the soft replicas of TX symbols and their MSEs to the soft IC.

E. EXTRINSIC VALUE EXCHANGE BASED ON EP

In this subsection, we describe the extrinsic value exchange via MM, according to the block diagram of EP-based IDD shown in Fig. 2(b). The procedure up to the generation of the posterior LLR $\boldsymbol{\alpha}_m$ is the same as SC/MMSE turbo equalization described in Section III-C; however, the subsequent extrinsic value generation process is different.

First, the posterior LLR $\boldsymbol{\alpha}_m$ in (13) is fed directly into the soft RG in Alg. 3 to obtain the posterior estimate $\acute{x}_{m,k}$ and its MSE $\acute{\phi}_{m,k}$. Next, the conditional PDF of the soft replica $\acute{x}_{m,k}$, given the true TX symbol $x_{m,k}$, is approximated by the Gaussian distribution with the expectation $\acute{x}_{m,k}$ and MSE $\acute{\phi}_{m,k}$ so as to minimize the Kullback-Leibler divergence (KLD). When approximating an arbitrary target distribution with a tractable distribution belonging to the exponential family so as to minimize KLD, it has been proven that it is sufficient to match the moments of the two distributions; hence, this operation is referred to as *moment matching (MM)* [35], [36]. Since this method adopts Gaussian as a tractable distribution, we need only adjust its mean (expected value) and the MSE equal, *i.e.*,

$$C\exp\left[-\frac{\left|x_{m,k} - \acute{x}_{m,k}\right|^2}{\acute{\phi}_{m,k}}\right] = \exp\left[-\frac{\left|x_{m,k} - \hat{x}_{m,k}\right|^2}{\hat{\phi}_{m,k}}\right]\exp\left[-\frac{\left|x_{m,k} - \bar{x}_{m,k}\right|^2}{\bar{\phi}_{m,k}}\right], \quad (19)$$

where $C \in \mathbb{R}$ denotes the proportionality constant. By solving (19) for $\hat{x}_{m,k}$ and $\hat{\phi}_{m,k}$, the extrinsic soft replica and its MSE can be expressed as [34], [36]

$$\hat{x}_{m,k} = \hat{\phi}_{m,k}\left(\frac{\acute{x}_{m,k}}{\acute{\phi}_{m,k}} - \frac{\bar{x}_{m,k}}{\bar{\phi}_{m,k}}\right), \quad (20a)$$

$$\frac{1}{\hat{\phi}_{m,k}} = \frac{1}{\acute{\phi}_{m,k}} - \frac{1}{\bar{\phi}_{m,k}}. \quad (20b)$$

F. ALGORITHM DESCRIPTION

The pseudocode of the IDD-based MUD algorithm described above is summarized in Alg. 4. The algorithm has a common SC/MMSE detection and channel decoder error correction process, and branches at the extrinsic value generation section. In SC/MMSE turbo equalization, the extrinsic value is generated in the LLR domain by subtracting the prior LLR from the posterior LLR in line 10. In contrast, in EP-based IDD, the extrinsic value is generated by subtracting the prior soft estimate from the posterior soft estimate according to their MSEs in lines 14 and 15. Unlike the SC/MMSE turbo equalization, which simplifies extrinsic value generation by assuming the consistency condition, EP-based IDD differs significantly in that it generates extrinsic values by matching the second moments of messages in the symbol domain.

TABLE 1. Simulation conditions.

Item	Value
MIMO configuration	$(N, M) = (32, 16), (32, 24), (32, 32)$
Channel estimation	Ideal estimation
Number of subcarriers	$L = 81$
Number of FFT point	128
Channel model	Rayleigh fading with equal powered 3-tap PDP
Modulation Scheme	Gray coded QPSK, 16QAM, 256QAM
Channel coding scheme	LDPC [65]
Channel decoding scheme	SPA
Code length	$N_c = 1944$
Code rate	$r_c = 2/3$
Maximum number of SPA iterations	$T_{SPA} = 50$
Number of IDD iteration	$T = 8$

G. BER PERFORMANCE

We have simulated a large MU-MIMO-OFDM system to compare the BER performance of SC/MMSE turbo equalization (turbo EQ) and EP-based IDD. The simulation conditions are summarized in Tab. 1. The frequency-selective channels are characterized by Rayleigh fading with an equal

[3]The idealized LLR that satisfies the consistency condition has a mean-to-variance ratio of 1:2.

Algorithm 4 IDD-Based MUD Algorithm

Require: $\{\boldsymbol{y}_k, \boldsymbol{H}_k, \forall k\}$, T (Num. of iterations)
Ensure: $\{\boldsymbol{\alpha}_m^{\prime(T)}, \forall m\}$

/* ——— Initialization ——— */
$\forall m, k$: $\hat{x}_{m,k}^{(1)} = \mathbb{E}[x_{m,k}] = 0$
$\forall m, k$: $\hat{\phi}_{m,k}^{(1)} = \mathbb{E}\left[\left|x_{m,k} - \hat{x}_{m,k}^{(1)}\right|^2\right] = E_{\mathrm{s}}$
/* ——— IDD Iteration ——— */
for $t = 1$ to T **do**
  // SC/MMSE detection and channel decoding
  $\forall k$: Execute Alg. 1 to obtain $\{\bar{x}_{m,k}^{(t)}, \bar{\phi}_{m,k}^{(t)}, \forall m\}$ using $\boldsymbol{y}_k$, $\boldsymbol{H}_k$, $\{\hat{x}_{m,k}^{(t)}, \hat{\phi}_{m,k}^{(t)}, \forall m\}$
  $\forall m$: Execute Alg. 2 to obtain $\{\bar{\boldsymbol{\beta}}_m^{(t)}, \forall m\}$ using $\{\bar{x}_{m,k}^{(t)}, \bar{\phi}_{m,k}^{(t)}, \forall k\}$
  $\forall m$: $\bar{\boldsymbol{\beta}}_m^{\prime(t)} = \Pi^{-1}\left(\bar{\boldsymbol{\beta}}_m^{(t)}\right)$
  $\forall m$: Execute error correction of $\bar{\boldsymbol{\beta}}_m^{\prime(t)}$ by decoder to obtain $\boldsymbol{\alpha}_m^{\prime(t)}$
  $\forall m$: $\boldsymbol{\alpha}_m^{(t)} = \Pi\left(\boldsymbol{\alpha}_m^{\prime(t)}\right)$
  // Extrinsic value generation and soft RG
  if Extrinsic LLR-based scheme **then**
  // SC/MMSE turbo Equalization
  $\forall m$: $\hat{\boldsymbol{\lambda}}_m^{(t)} = \boldsymbol{\alpha}_m^{(t)} - \bar{\boldsymbol{\beta}}_m^{(t)}$
  $\forall m$: Execute Alg. 3 to obtain $\{\hat{x}_{m,k}^{(t+1)}, \hat{\phi}_{m,k}^{(t+1)}, \forall k\}$ using $\hat{\boldsymbol{\lambda}}_m^{(t)}$
  else
  // EP-based IDD
  $\forall m$: Execute Alg. 3 to obtain $\{\acute{x}_{m,k}^{(t)}, \acute{\phi}_{m,k}^{(t)}, \forall k\}$ using $\boldsymbol{\alpha}_m^{(t)}$
  $\forall m, k$: $\frac{1}{\hat{\phi}_{m,k}^{(t+1)}} = \frac{1}{\acute{\phi}_{m,k}^{(t)}} - \frac{1}{\bar{\phi}_{m,k}^{(t)}}$
  $\forall m, k$: $\hat{x}_{m,k}^{(t+1)} = \hat{\phi}_{m,k}^{(t+1)}\left(\frac{\acute{x}_{m,k}^{(t)}}{\acute{\phi}_{m,k}^{(t)}} - \frac{\bar{x}_{m,k}^{(t)}}{\bar{\phi}_{m,k}^{(t)}}\right)$
  end if
end for

powered three-tap power delay profile (PDP). The system employs 81 subcarriers, and the number of FFT points is set to 128. The average RX power from each TX antenna is assumed to be identical based on the slow open-loop TX power control, and the time and frequency synchronization is assumed to be perfect. The MIMO-OFDM channel is assumed to be estimated at the receiver without error, and its entries, *i.e.*, the fading coefficients, are assumed to be constant for each R time slot transmission. The modulation schemes are Gray-coded QPSK, 16QAM, and 256QAM.[4] The low-density parity-check (LDPC) code with the rate of $r_{\mathrm{c}} = 2/3$ and length $N_{\mathrm{c}} = 1944$ coded bits used in the IEEE 802.11n standard is used as the channel code [65]. The sum-product algorithm (SPA) is used in the channel decoder, where the decoding process is terminated when either satisfying all parity checks or reaching the predetermined maximum number of SPA iterations $T_{\mathrm{SPA}} = 50$. The maximum number of IDD iterations is set to $T = 8$.

Fig. 3 shows the BER performance as a function of signal-to-noise power ratio (SNR), defined as SNR $\triangleq ME_{\mathrm{s}}/N_0$, in the large MU-MIMO-OFDM systems with $(N, M) = (32, 16)$, $(32, 24)$, and $(32, 32)$, respectively. Note that the performance of the two methods should agree for the first iteration ($T = 1$) since their operation are identical.

In the configuration of $(N, M) = (32, 16)$ in Figs. 3(a)-(c), the number of RX antennas N is sufficiently larger than the number of spatial multiplexing M, so the accuracy of SC/MMSE detection is sufficiently high due to channel hardening [18]. In this case, especially for QPSK modulation, the LLR meets the consistency condition with high accuracy; hence, it is possible to appropriately generate and exchange extrinsic values in the LLR domain. Consequently, as illustrated in Fig. 3(a), the performance of turbo EQ and EP-based IDD appear to be comparable. On the other hand, when using a non-orthogonal mapping rule, as the modulation order Q increases, the actual LLR behavior gradually deviates from the statistical properties of the idealized LLR that meets the consistency condition. In fact, in Figs. 3(b) and (c), EP-based IDD achieves better performance than turbo EQ, and the performance difference is more pronounced for 256QAM. The results suggest that extrinsic value generation in the symbol domain via MM is not affected by inter-bit correlation, and that it can achieve robust extrinsic value exchange in higher-order modulation transmission.

Next, in the configuration of $(N, M) = (32, 24)$ in Figs. 3(d)-(f), the performance of EP-based IDD is significantly better than that of turbo EQ. The improvement is particularly noticeable for the higher-order modulation schemes, where the performance difference at BER $= 10^{-4}$ for $T = 8$ is about 1.2 dB in Fig. 3(e) and about 1.5 dB in Fig. 3(f). As the spatial load increases, the SC/MMSE detection accuracy decreases, making it difficult to appropriately exchange extrinsic values in the LLR domain, and we can see that the iterative gain after the 4-th iteration becomes small in turbo EQ. On the other hand, the iterative gain is maintained in EP-based IDD, which supports the success of extrinsic value exchange via MM.

Finally, in the configuration of $(N, M) = (32, 32)$ in Figs. 3(g)-(i), it becomes difficult to suppress interference using SC/MMSE detection, and the residual interference components violate the consistency condition as correlated noise; hence, extrinsic value exchange in the LLR domain does not work well. As a result, the performance difference between turbo EQ and EP-based IDD increases to about 1.2 dB for QPSK in Fig. 3(g), about 2.5 dB for 16QAM in Fig. 3(h), and about 5 dB for 256QAM in Fig. 3(I) at BER $= 10^{-4}$ for $T = 8$.

[4]The performance of 64QAM is omitted due to the space limitation.

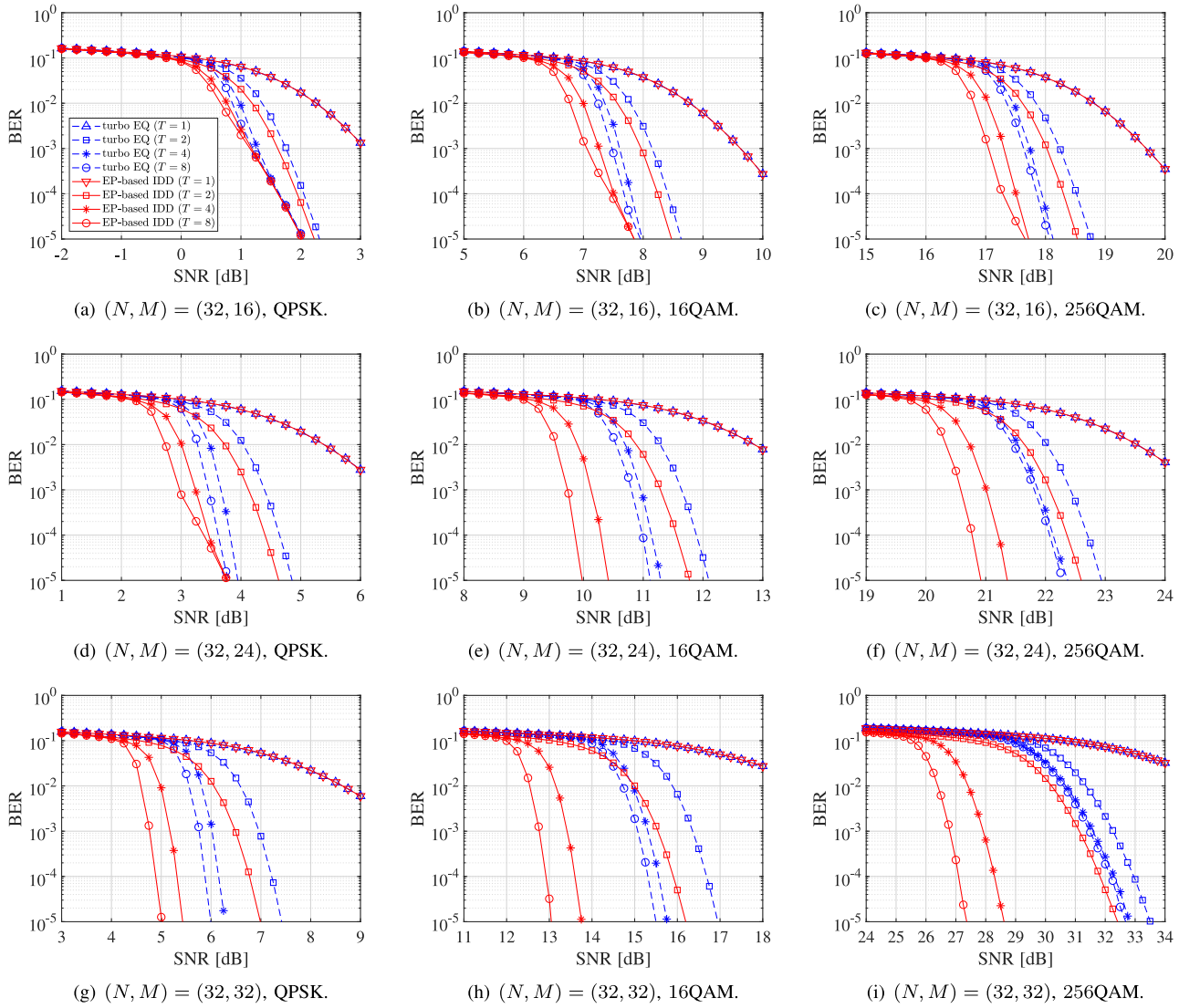

(a) $(N, M) = (32, 16)$, QPSK. (b) $(N, M) = (32, 16)$, 16QAM. (c) $(N, M) = (32, 16)$, 256QAM.

(d) $(N, M) = (32, 24)$, QPSK. (e) $(N, M) = (32, 24)$, 16QAM. (f) $(N, M) = (32, 24)$, 256QAM.

(g) $(N, M) = (32, 32)$, QPSK. (h) $(N, M) = (32, 32)$, 16QAM. (i) $(N, M) = (32, 32)$, 256QAM.

FIGURE 3. BER performance versus SNR for various MIMO configurations and modulation schemes.

The aforementioned numerical results indicate that an increase in modulation order and spatial load enhances the robustness and efficacy of the iterative process for exchanging extrinsic values in the symbol domain through MM, as opposed to those in the LLR domain via extrinsic LLR.

IV. EXIT CHART ANALYSIS FOR EP-BASED IDD

The EXIT chart is an analytical technique that assesses, both visually and numerically, the degree of knowledge about the intended (target) signal that may be acquired at each iteration step of IDD, by treating the transfer of extrinsic information between modules as an exchange of MI. By plotting the input-output relationship of MI for each module as an EXIT function (*curve*), and by tracing the evolution of MI during actual iterative processing as an EXIT *trajectory*, the iterative behavior of IDD can be systematically analyzed [39], [40].

To visualize the exchange of extrinsic values in the EXIT chart, it is necessary to appropriately divide the IDD algorithm into two modules. In this paper, each IDD algorithm is divided as illustrated in Fig. 4, where the blue dashed line indicates the division line: the side including the SC/MMSE detector is defined as Module A, while the side including the channel decoder is defined as Module B. By dividing the algorithm so that the extrinsic value generation mechanism is included within Module B, the information flowing through the division point becomes extrinsic values.[5] The module division for SC/MMSE turbo equalization in Fig. 4(a) is exactly the same as that used in previous EXIT chart analysis [45], [46], [47].

When applying EXIT chart analysis, the fundamental difference between the two IDD algorithms lies in the type of information exchanged across the division point. In SC/MMSE turbo equalization, LLRs are exchanged, whereas in EP-based IDD, the exchanged information consists of

[5]For both IDD algorithms, the two module division points are logically identical: 1) after SC/MMSE detection, and 2) after extrinsic value generation by subtracting prior information from posterior information.

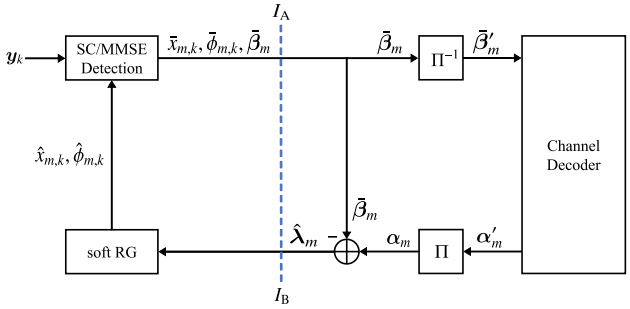

(a) SC/MMSE turbo equalization.

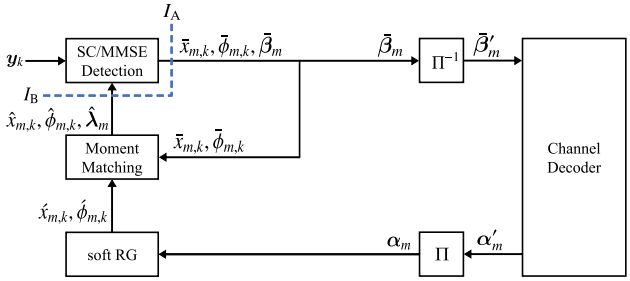

(b) EP-based IDD.

FIGURE 4. Module division for EXIT chart analysis.

symbol estimates and their associated MSEs. The fact that the information exchanged at the division points is defined in the symbol domain introduces two inherent challenges for constructing the EXIT curves:

- *MI loss during the conversion from bit-wise LLRs to symbol estimates under high-order modulation:* In the case of Gray-coded QPSK, where the bit-to-symbol mapping is orthogonal,[6] a sequence of symbol estimates can be generated that preserves the MI of the original bit-wise LLR sequence. However, for higher-order QAMs (*e.g.*, $Q \geq 16$), the bit-to-symbol mapping becomes non-orthogonal, and converting from bit-wise LLRs to symbol estimates introduces MI loss. If this loss is not properly accounted for, the resulting EXIT curves will fail to accurately capture the actual iterative behavior of EP-based IDD.
- *Proper modeling of the input symbol estimates (i.e., their associate statistics) for each module:* In the case of SC/MMSE turbo equalization, modeling the input and output of each module is straightforward because the exchanged information is represented by LLRs. Under the assumption that the consistency condition holds, it is known that a bit-wise LLR sequence with arbitrary MI can be generated using the J-function [39], making the construction of module inputs relatively easy. In contrast, for EP-based IDD, the symbol estimates and their associated MSEs input to each module during the iterative process exhibit fundamentally different statistical properties depending on how they are generated. It is not difficult to imagine that the statistical properties of the symbol estimates output from the SC/MMSE detector (*i.e.*, a linear filter) differ significantly from those output from the soft RG (*i.e.*, a nonlinear denoiser).

In the following subsections, we provide a detailed description of these challenges and their corresponding solutions. We then describe the procedure for plotting the EXIT curves for each module in the EP-based IDD.

[6] *Orthogonal mapping* refers to a mapping scheme in which each bit is uniquely and independently assigned to either the in-phase or quadrature component of a modulated symbol.

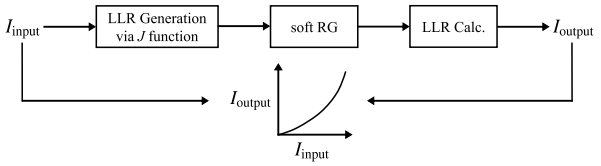

FIGURE 5. MI measurement before and after conversion to symbol estimates.

A. MI LOSS DURING CONVERSION FROM BIT-WISE LLRs TO SYMBOL ESTIMATES

This section describes the MI loss that occurs during the conversion from bit-wise LLRs to symbol estimates when high-order modulation schemes are employed. Hereafter, the MI used in this paper refers to the well-known bit-wise MI defined between the TX bit and the corresponding bit-wise LLR, as presented in [39].

As illustrated in Fig. 5, an LLR with an arbitrary input MI I_{inout} is generated using the J function [39], [40]. Then, by computing the conditional expectation of the TX symbol given the LLRs, the corresponding soft symbol estimates and their MSEs are obtained. Subsequently, they are converted back into bit-wise LLRs, and the resulting output MI I_{output} is measured. By comparing the input MI I_{inout} with the measured output MI I_{output}, the MI loss introduced during the conversion process can be quantitatively evaluated.

Fig. 6 shows the relationship between the input MI I_{input} before symbol conversion and the output MI I_{output} after symbol conversion for various modulation schemes. Gray-coded QPSK, 16QAM, 64QAM, and 256QAM were used as the modulation schemes. The output MI was computed using the LLR sequence corresponding to 10^6 symbols. The results show that, for QPSK, the input and output MI are approximately equal[7] (*i.e.*, $I_{\text{input}} \approx I_{\text{output}}$). In contrast, for higher-order modulations ($Q \geq 16$), a significant decrease is observed in the output MI compared to the input MI (*i.e.*, $I_{\text{input}} > I_{\text{output}}$). This phenomenon occurs because, in higher-order modulations, both the real and imaginary parts of a symbol are determined by multiple bits, introducing dependencies among the constituent bits (*i.e.*, inter-bit correlations). The conversion from independently generated bit-wise LLRs to symbol estimates induces such correlations, resulting in MI loss.

[7] Even with QPSK modulation, a slight MI loss occurs due to the finite number of LLR samples used for MI measurement, which limits the accuracy of the resulting histogram.

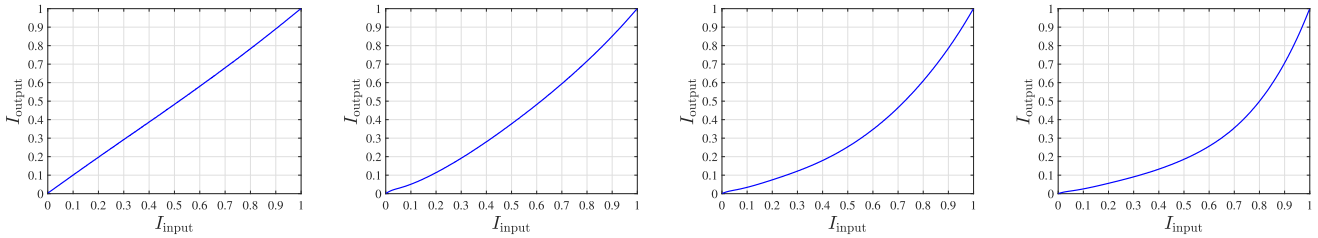

(a) QPSK. (b) 16QAM. (c) 64QAM. (d) 256QAM.

FIGURE 6. MI loss during the conversion from bit-wise LLRs to symbol estimates.

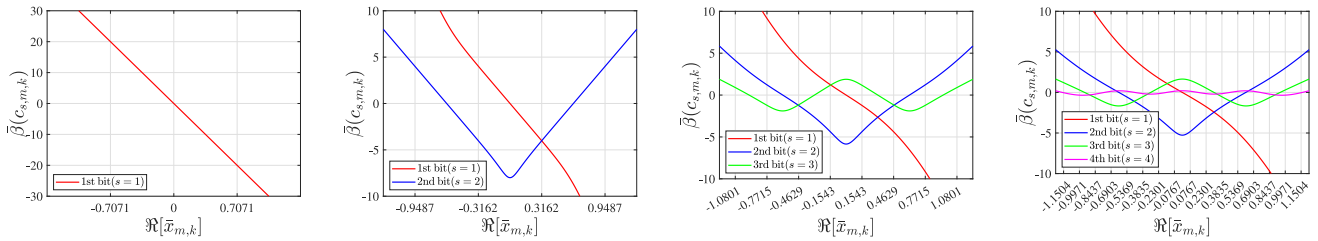

(a) QPSK. (b) 16QAM. (c) 64QAM. (d) 256QAM.

FIGURE 7. Projection function from the real part of a symbol estimate to bit-wise LLRs ($E_s/\bar{\phi}_{m,k} = 10$ [dB]).

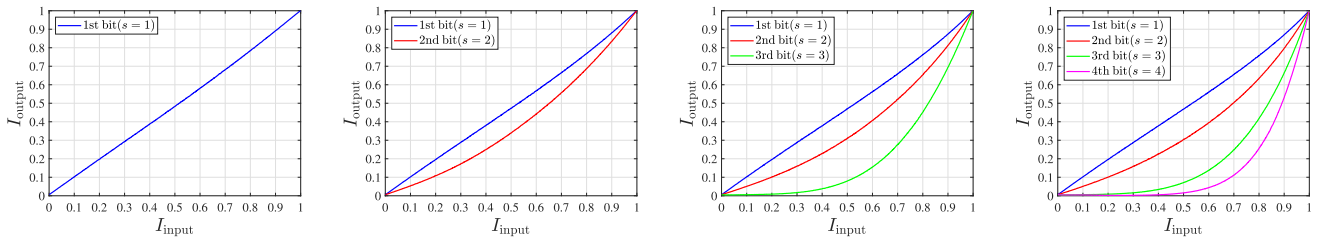

(a) QPSK. (b) 16QAM. (c) 64QAM. (d) 256QAM.

FIGURE 8. MI loss during the conversion from bit-wise LLRs to symbol estimates per each bit position.

To gain a more intuitive understanding of how this MI loss arises, we analyze the input–output relationship of (9), which converts symbol estimates and their MSEs into bit-wise LLRs. For simplicity, we focus on the real part of the symbol estimates, *i.e.*, $\Re[\bar{x}_{m,k}], \forall m, k$, leveraging the orthogonality between the real and imaginary components in Gray-coded QAM. It is worth noting that a similar discussion applies to the imaginary parts $\Im[\bar{x}_{m,k}], \forall m, k$, as well.

Fig. 7 shows the projection function from the real part of the symbol estimate $\Re[\bar{x}_{m,k}]$ to the bit-wise LLRs $\bar{\beta}(c_{1,m,k}), \bar{\beta}(c_{2,m,k}), \ldots, \bar{\beta}(c_{S,m,k})$ for each bit position, based on (9), under various modulation schemes. The horizontal axis represents the value of $\Re[\bar{x}_{m,k}]$, and the vertical axis represents the corresponding bit-wise LLR $\bar{\beta}(c_{s,m,k})$. The grid along the horizontal axis corresponds to the real part of the QAM constellation points, assuming an average symbol energy of $E_{\text{s}} = 1$. A key observation from these results is that, while the projection function for the first-bit position is a monotonic function in all modulation schemes, the functions corresponding to the second and subsequent bits exhibit local maxima and minima. This indicates that the dynamic range of the resulting bit-wise LLRs is limited depending on the bit position. Ideally, bit-wise LLRs–which convey the *reliability* of each estimated bit–should span the entire real line, as in the case for the input LLRs generated via J function. However, the LLRs reconstructed from symbol estimates exhibit restricted dynamic ranges, leading to a loss of information regarding bit reliability. This fact confirms that the conversion from bit-wise LLRs to symbol estimates via (15) is non-invertible, and that re-conversion from the symbol estimates to bit-wise LLRs does not preserve the original MI.

The impact of the limited dynamic range of LLRs observed in Fig. 7 can also be visualized in the MI domain by focusing on the bit positions. Fig. 8 shows the relationship between I_{input} and I_{output} when MI is independently measured for each bit position within the real part of a QAM symbol. For instance, in the case of 16QAM, the real part of each symbol consists of 2 bits. In Fig. 8(b), the "1st bit" refers to the MI measured using only the LLRs corresponding to the first bit ($s = 1$), while the "2nd bit" refers to that measured using only the LLRs corresponding to the second bit ($s = 2$). It should be noted the average MI across all bit positions matches the result shown in Fig. 6. As the restriction in the

LLR dynamic range becomes more pronounced in Fig. 7, the MI degradation observed in Fig. 8 increases accordingly. This effect is particularly noticeable in the later bit positions of each symbol, where the dependency on preceding bits is greater.

The above analysis has clarified that, when high-order modulation is used, MI loss occurs during the conversion from bit-wise LLRs to symbol estimates. In EP-based IDD, symbol estimates and their MSEs are exchanged between two modules as the extrinsic information. Hence, if symbol-domain inputs are simply generated by converting an LLR sequence with a given MI, the resulting MI in the symbol domain will differ from that in the LLR domain, making accurate analysis impossible. Unless the inputs to each module are properly modeled to reflect what is expected during actual iterative processing, the EXIT curves cannot be accurately plotted. In such a case, the resulting EXIT curves will inevitably be inconsistent with the EXIT trajectory.

The most effective way to address this challenge in EXIT chart analysis for EP-based IDD is to retain both the symbol estimates/MSEs and the corresponding bit-wise LLRs as the extrinsic information exchanged between two modules. Specifically, as illustrated in Fig. 4(b), it is assumed that the information flowing through the connections in the block diagram of the IDD algorithm simultaneously carries MIs corresponding to both the LLRs and the symbol estimates/MSEs. The appropriate representation can be selectively used depending on the operation, thereby avoiding breakdowns in the analysis. This approach eliminates the need to explicitly consider LLR-to-symbol conversions in the subsequent analysis, thus enhancing the clarity and tractability of the EXIT chart analysis for EP-based IDD. Based on this approach, the following subsection presents a method for appropriately modeling the input symbol estimates for each module and constructing the EXIT curves.

B. MODELING INPUT SYMBOL ESTIMATES AND CONSTRUCTING EXIT CURVES

This section describes the method for appropriately modeling the input symbol estimates of each module and constructing the corresponding EXIT curves.

Module A: Fig. 9(a) illustrates the modeling approach for the input symbol estimates of Module A. During the iterative process of IDD, the input to Module A corresponds to the symbol estimates output from the nonlinear denoiser, highlighted in orange. It should be noted that, although MM corrects only up to the second-order statistics, the actual stochastic behavior of the equivalent noise is governed by the non-linearity of soft replica generator (soft RG). Therefore, to accurately model this nonlinear noise, we directly input the LLR sequence into soft RG and use the resulting soft estimates and their MSEs–computed based on the conditional expectation–as the model for the input information to Module A.

Fig. 9(b) illustrates a block diagram of the procedure for measuring the input and output MI of Module A. The

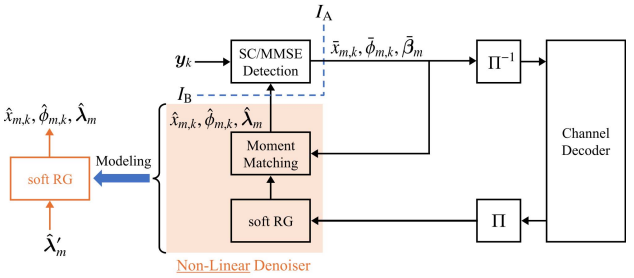

(a) Modeling input symbol estimates of module A.

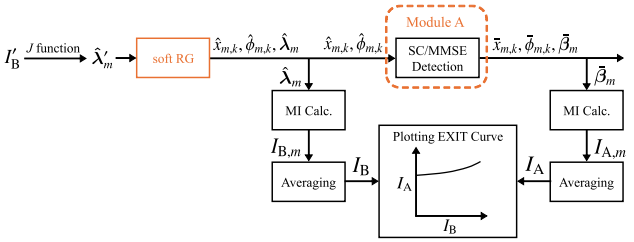

(b) Measuring module input and output MI

FIGURE 9. Schematic diagram for modeling the input symbol estimates of module A and plotting the EXIT curve.

region enclosed by the orange dashed line represents the processing of Module A, and the MI is measured for the symbol estimate sequences at the input and output of this module. The soft RG module used to generate the input symbol estimates and their MSEs–modeled as described in Fig. 9(a)–is shown as the orange-colored block. Based on this block diagram, the procedure for measuring the input and output MI of Module A is described step-by-step below.

First, a bit-wise LLR sequence $\hat{\boldsymbol{\lambda}}'_m, \forall m$, is generated using the J function such that it has a target MI I'_{B}. Then, using Alg. 3, the corresponding soft estimates $\hat{x}_{m,k}, \forall m, k$, and their MSEs $\hat{\phi}_{m,k}, \forall m, k$, are computed. From these, the associated LLR sequence $\hat{\boldsymbol{\lambda}}_m, \forall m$, is measured using Alg. 2. The resulting symbol estimates are then fed back to the SC/MMSE detector. Using the corresponding LLR sequence $\hat{\boldsymbol{\lambda}}_m$, the MI of the soft symbol sequence input to Module A, $I_{\mathrm{B},m}$, is measured for each stream m. By averaging over all M streams, the average input MI for Module A is obtained as $I_{\mathrm{B}} = 1/M \sum_{m=1}^{M} I_{\mathrm{B},m}$. By measuring the MI of the LLR sequence corresponding to the input symbol estimates, an appropriate input MI for the module is obtained.

Next, using the symbol estimates input to Module A, the SC/MMSE detection is performed according to Alg. 1, resulting in the detected symbols $\bar{x}_{m,k}, \forall m, k$, and their MSEs $\bar{\phi}_{m,k}, \forall m, k$. Subsequently, the LLR sequences $\bar{\boldsymbol{\beta}}_m, \forall m$, are computed based on the detected symbols using Alg. 2. The output MI $I_{\mathrm{A},m}$ for each stream m is then measured based on the histogram of the corresponding LLR sequence [28]. Similarly, by averaging these values across all M streams, the average output MI I_{A} is obtained.

In fact, the MI of the detector output differs across streams. However, in this paper, we assume that the quality of each TX stream is statistically uniform from the perspective

Algorithm 5 EXIT Curve for Module A in EP-Based IDD

Require: Tentative Input MI I'_{B}, coded bits $\{\boldsymbol{c}_m, \forall m\}$, channel matrix and corresponding RX vector $\{\boldsymbol{H}_k, \boldsymbol{y}_k, \forall k\}$
Ensure: Input MI I_B, Output MI I_{A}

/* ———— Initialization ———— */
$\sigma_{\mathrm{B}} = J^{-1}(I'_{\mathrm{B}})$, $\mu_{\mathrm{B}} = \frac{\sigma_{\mathrm{B}}^2}{2}$
$\forall m : \hat{\boldsymbol{\lambda}}'_m = \mu_{\mathrm{B}}\boldsymbol{c}_m + \boldsymbol{\nu}_{\mathrm{B}}$,
where each entry of $\boldsymbol{\nu}_{\mathrm{B}}$ follows $\mathcal{CN}(0, \sigma_{\mathrm{B}}^2)$
/* ———— Soft RG ———— */
$\forall m$: Execute Alg. 3 to obtain $\{\hat{x}_{m,k}, \hat{\phi}_{m,k}, \forall k\}$
using $\hat{\boldsymbol{\lambda}}'_m$
/* ———— Input MI calculation ———— */
$\forall m$: Execute Alg. 2 to obtain $\hat{\boldsymbol{\lambda}}_m$
using $\{\hat{x}_{m,k}, \hat{\phi}_{m,k}, \forall k\}$
$\forall m$: $I_{\mathrm{B},m}$ is calculated from the histogram of $\hat{\boldsymbol{\lambda}}_m$ [28]
$I_{\mathrm{B}} = \frac{1}{M}\sum_{m=1}^{M} I_{\mathrm{B},m}$
/* ———— SC/MMSE detection ———— */
$\forall k$: Execute Alg. 1 to obtain $\{\bar{\boldsymbol{x}}_m, \bar{\boldsymbol{\phi}}_m, \forall m\}$
using $\boldsymbol{y}_k$, $\boldsymbol{H}_k$, $\{\hat{x}_{m,k}, \hat{\phi}_{m,k}, \forall m\}$
$\forall m$: Execute Alg. 2 to obtain $\bar{\boldsymbol{\beta}}_m$
using $\{\bar{x}_{m,k}, \bar{\phi}_{m,k}, \forall k\}$
/* ———— Output MI calculation ———— */
$\forall m$: $I_{\mathrm{A},m}$ is calculated from the histogram of $\bar{\boldsymbol{\beta}}_m$ [28]
$I_{\mathrm{A}} = \frac{1}{M}\sum_{m=1}^{M} I_{\mathrm{A},m}$

of long-term statistics due to *channel hardening* in large MIMO channels [18], based on the premise of slow power control at the transmitter side. Under this assumption, the MI is calculated by averaging across streams. The resulting MI represents the *average* input-output relationship of the channel decoder and sufficient knowledge for performing iterative convergence analysis using EXIT chart.

The above procedure is summarized in pseudocode form as Alg. 5. For EXIT curve construction, as illustrated in 9(b), the average input MI I_{B} is plotted on the horizontal axis, and the average output MI I_{A} is plotted on the vertical axis. By measuring pairs of input and output MI $(I_{\mathrm{B}}, I_{\mathrm{A}})$ for various values of the parameterized tentative input MI I'_{B}, the input-output relationship of Module A can be visualized as an EXIT curve.

Module B: Fig. 10(a) illustrates the modeling approach for the symbol estimates input to Module B. During the iterative process of IDD, the input to Module B corresponds to the symbol estimates output from the SC/MMSE detector, highlighted in green. Unlike the input to Module A, which consists of the soft replicas generated through nonlinear processing (*i.e.*, denoiser), the input to Module B results from linear processing (*i.e.*, LMMSE filtering). It is well known that the output of the LMMSE filter can be well approximated as the output of an equivalent AWGN channel [36], [66]. Therefore, the input to Module B can be

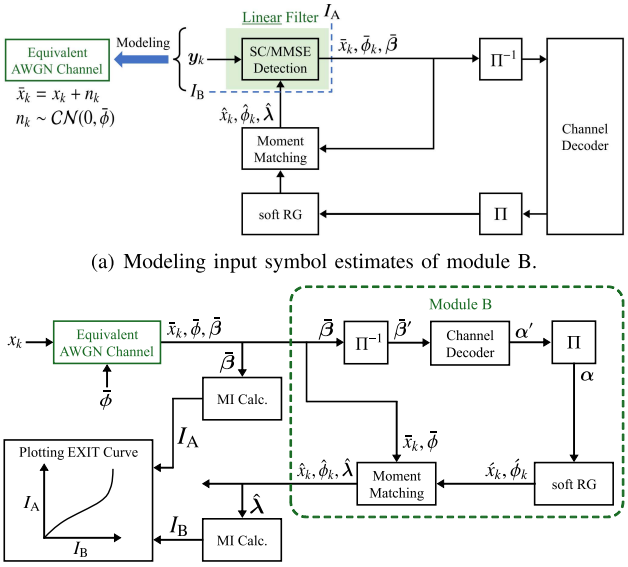

FIGURE 10. Schematic diagram for modeling the input symbol estimates of module B and plotting the EXIT curve.

modeled as symbols observed through an equivalent AWGN channel with a given input variance $\bar{\phi}$, representing the MSE of the SC/MMSE-detected symbols.

Fig. 10(b) illustrates the block diagram for measuring the input and output MI of Module B. The region enclosed by the green dashed lines represents the processing of Module B, and the MI is measured for the symbol estimate sequences at the input and output of this module. Based on this block diagram, the procedure for measuring the input and output MI of Module B is described step-by-step below.

First, the TX symbol sequence $x_k, \forall k$, is passed through an equivalent AWGN channel with variance $\bar{\phi}$ to generate a pseudo output of the SC/MMSE detector, given by $\bar{x}_k = x_k + n_k, \forall k$, where $n_k \sim \mathcal{CN}(0, \bar{\phi})$. Then, the corresponding LLR sequence $\bar{\boldsymbol{\beta}}$ is computed using Alg. 2. The MI of $\bar{\boldsymbol{\beta}}$ is measured and used as the input MI I_{A} for Module B. The generated soft symbol sequence will also be used as prior information in the subsequent extrinsic value generation process, as described later.

Next, the LLR sequence $\bar{\boldsymbol{\beta}}$ undergoes de-interleaving and is input to the channel decoder for error correction. The decoder outputs the posterior LLR sequence $\boldsymbol{\alpha}'$, which is then interleaved to obtain $\boldsymbol{\alpha}$. Using this posterior LLR sequence, soft replicas $\acute{x}_k, \forall k$, and their MSEs $\acute{\phi}_k, \forall k$, are generated via Alg. 3. These soft replicas are used as posterior information in symbol-domain extrinsic value generation. Given the prior information $\bar{x}_k, \forall k$, and $\bar{\phi}$, along with the posterior information, the extrinsic symbol estimates $\hat{x}_k, \forall k$, and their MSEs $\hat{\phi}_k, \forall k$, are generated through MM in (20). The resulting extrinsic symbol estimate sequence is then converted into the corresponding LLR sequence $\hat{\boldsymbol{\lambda}}$ using Alg. 2. Finally, the output MI I_{B} is obtained based on the histogram of $\hat{\boldsymbol{\lambda}}$.

Algorithm 6 EXIT Curve for Module B in EP-Based IDD

Require: Input AWGN variance $\bar{\phi}$, coded bits $\boldsymbol{c}$
Ensure: Input MI I_{A}, Output MI I_{B}

/* ———— Initialization ———— */
Modulate $\boldsymbol{c}$ to obtain $\boldsymbol{x} \triangleq [x_1, \ldots, x_k, \ldots, x_K] \in \mathbb{C}^{1\times K}$
$\forall k$: $\bar{x}_k = x_k + v_{m,k}$, $v_{m,k} \sim \mathcal{CN}(0, \bar{\phi})$
/* ———— Input MI calculation ———— */
Execute Alg. 2 to obtain $\bar{\boldsymbol{\beta}}$ using $\{\bar{x}_k, \bar{\phi}, \forall k\}$
I_{A} is calculated from the histogram of $\bar{\boldsymbol{\beta}}$ [28]
/* ———— Channel decoding ———— */
$\bar{\boldsymbol{\beta}}' = \Pi^{-1}(\bar{\boldsymbol{\beta}})$
Execute error correction of $\bar{\boldsymbol{\beta}}'$ by decoder to obtain $\boldsymbol{\alpha}'$
$\boldsymbol{\alpha} = \Pi(\boldsymbol{\alpha}')$
/* —— Extrinsic value generation via MM —— */
Execute Alg. 3 to obtain $\{\acute{x}_k, \acute{\phi}_k, \forall k\}$ using $\boldsymbol{\alpha}$
$\forall k$: $\frac{1}{\hat{\phi}_k} = \frac{1}{\acute{\phi}_k} - \frac{1}{\bar{\phi}}$
$\forall k$: $\hat{x}_k = \hat{\phi}_k\left(\frac{\acute{x}_k}{\acute{\phi}_k} - \frac{\bar{x}_k}{\bar{\phi}}\right)$
/* ———— Output MI calculation ———— */
Execute Alg. 2 to obtain $\hat{\boldsymbol{\lambda}}$ using $\{\hat{x}_k, \hat{\phi}_k, \forall k\}$
I_{B} is calculated from the histogram of $\hat{\boldsymbol{\lambda}}$ [28]

The above procedure is summarized in pseudocode form as Alg. 6. For EXIT curve construction, as illustrated in Fig. 10(b), the input MI I_{A} is plotted on the vertical axis, and the output MI I_{B} is plotted on the horizontal axis. By varying the equivalent noise variance $\bar{\phi}$ of the AWGN channel and measuring pairs of input and output MI $(I_{\mathrm{A}}, I_{\mathrm{B}})$, the input-output relationship of Module B can be visualized as an EXIT curve.

As a final remark, we summarize the overall procedure of the EXIT chart analysis to conclude this subsection. In EXIT chart analysis, the EXIT curves of both modules are first plotted in advance, and the iterative convergence behavior is analyzed by overlaying the EXIT trajectory on top of these curves [39]. To construct the EXIT trajectory, the MI at the two division points shown in Fig. 4(b) is measured during each iteration of the actual IDD process. The MI pairs $(I_{\mathrm{B}}, I_{\mathrm{A}})$ at each division point are sequentially plotted, and by connecting the points starting from the first iteration as $(0, I_{\mathrm{A}})$, the EXIT trajectory is traced to visualize the iterative behavior of the algorithm.

C. EVALUATION VIA EXIT CHART ANALYSIS

Using the methods introduced above, we have conducted the EXIT chart analysis of EP-based IDD. The EXIT chart analysis of conventional SC/MMSE turbo equalization (turbo EQ) was performed following the standard procedures described in [45], [46], [47]. The simulation parameters are identical to those listed in Tab. 1 of Section III-G, and the EXIT chart analysis presented below corresponds to the BER performance shown in Fig. 3.

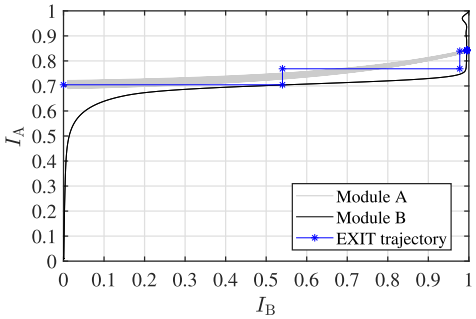

(a) turbo EQ, 16QAM at SNR = 8 dB.

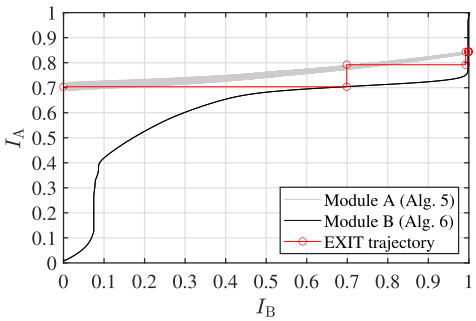

(b) EP-based IDD, 16QAM at SNR = 8 dB.

FIGURE 11. EXIT chart analysis for $(N,M) = (32,16)$.

Fig. 11 shows the EXIT chart for the $(N, M) = (32, 16)$ configuration with 16QAM signaling, corresponding to SNR = 8 dB in Fig. 3(b), where the horizontal and vertical axes represent I_{B} and I_{A}, respectively. The EXIT curves of Module A are generated for each of 100 realizations of $\{\boldsymbol{H}_k, \boldsymbol{y}_k, \forall k\}$ to verify the channel hardening effect, so they appear as gray bands. In the EP-based IDD case shown in Fig. 11(b), the EXIT curves of Module A are generated using Alg. 5, while those of Module B are generated using Alg. 6. The EXIT trajectory is plotted using one of the 100 realizations used to construct the EXIT curves of Module A and illustrates the MI evolution during iterative processing. Vertical movements along the trajectory indicate MI gains associated with Module A, while horizontal movements indicate MI gains associated with Module B. When the EXIT trajectory reaches $I_{\mathrm{B}} = 1$, full knowledge of the TX bits is acquired, allowing for error-free decoding. Conversely, in the event that the EXIT curves of Modules A and B intersect at a midpoint, the MI is unable to progress beyond this intersection point. The EXIT trajectory is consequently inhibited from attaining $I_{\mathrm{B}} = 1$, leading to the occurrence of decoding errors.

At the SNR = 8 dB point in Fig. 3(b), which corresponds to Fig. 11, both turbo EQ and EP-based IDD achieve BERs below 10^{-5}. Hence, a tunnel is opened between the EXIT curves of Modules A and B, and the EXIT trajectory is able to reach $I_{\mathrm{B}} = 1$. In Fig. 11, the EXIT curves and EXIT trajectory are in good agreement, and it can be seen that EXIT chart analysis can be achieved even with EP-based IDD by using the proposed method.

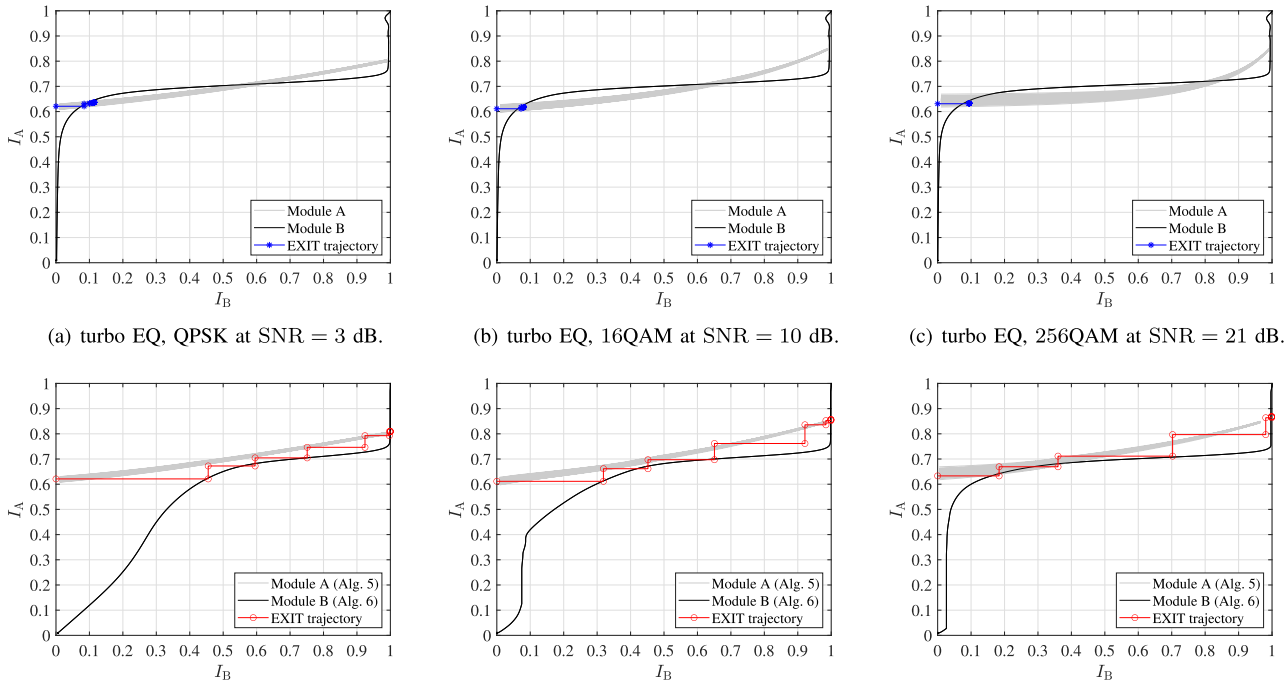

(a) turbo EQ, QPSK at SNR = 3 dB. (b) turbo EQ, 16QAM at SNR = 10 dB. (c) turbo EQ, 256QAM at SNR = 21 dB.

(d) EP-based IDD, QPSK at SNR = 3 dB. (e) EP-based IDD, 16QAM at SNR = 10 dB. (f) EP-based IDD, 256QAM at SNR = 21 dB.

FIGURE 12. EXIT chart analysis for $(N,M) = (32,24)$.

A notable observation here is that EP-based IDD exhibits a wider tunnel. This suggests that the generation of symbol-domain extrinsic values through MM, which accounts for the discrete constraints of symbols, can lead to a more robust MUD compared to the traditional extrinsic LLR-based approach. To validate this hypothesis, we shift our focus to MIMO configurations with higher spatial loading. Although some misalignment between the EXIT curves and trajectory may occur under these challenging conditions,[8] meaningful insights can still be extracted from the analysis results.

Fig. 12 shows the EXIT chart for the $(N, M) = (32, 24)$ configuration, corresponding to the BER performance shown in Figs. 3(d)-(f), respectively. Figs. 12(a)-(c) show the EXIT chart for turbo EQ, where the EXIT curves for all modulation schemes intersect. As a result, the EXIT trajectory cannot exceed the intersection point, indicating that the MUD performance does not improve even as the number of IDD iterations T increases. These observations are consistent with the BER performance shown in Figs. 3(d)-(f), where the performance improvement saturates around BER $= 10^{-2}$ at the specified SNR points. In contrast, the EXIT charts for EP-based IDD shown in Figs. 12(d)-(f) reveal that a tunnel remains open between the EXIT curves of Modules A and B, allowing the EXIT trajectory to reach around $I_B = 1$. These results align with the BER performance in Figs. 3(d)-(f); specifically, in Fig. 3(d), MUD achieves a BER below 10^{-3}, while in Figs. 3(e) and (f), nearly error-free MUD performance is achieved.

Fig. 13 presents the EXIT chart for a highly spatially loaded MIMO configuration, specifically for the $(N, M) = (32, 32)$ setup, which corresponds to the BER performance shown in Fig. 3(g)-(i). From these results, similar insights to those in Fig. 12 can be drawn. Although the consistency between the EXIT curves and the EXIT trajectory is reduced under this highly spatially loaded configuration, it remains feasible to validate the effectiveness of symbol-domain extrinsic value generation via MM in EP-based IDD.

The results presented above substantiate the findings derived from the BER performance comparisons. It is evident that an increase in modulation order and spatial load enhances the robustness and effectiveness of the iterative process involved in the exchange of extrinsic values within EP-based IDD, in contrast to turbo equalization.

V. EVALUATION UNDER CORRELATED CHANNELS

Finally, to compare the two IDD algorithms under more realistic channel conditions and to validate the robustness of the proposed framework of EXIT chart analysis, we conducted numerical simulations over correlated MIMO channels, where spatial correlation exists among the fading coefficients.

A. CHANNEL MODEL

We adopted the well-known Kronecker model [18] to represent spatial correlation and evaluated the signal detection performance in correlated MIMO channels. Under

[8]This phenomenon occurs because, as the detection problem becomes more challenging, the SC/MMSE detection accuracy deteriorates, leading to a growing discrepancy between the ideal behavior assumed when plotting the EXIT curves and the actual iterative behavior traced by the EXIT trajectory.

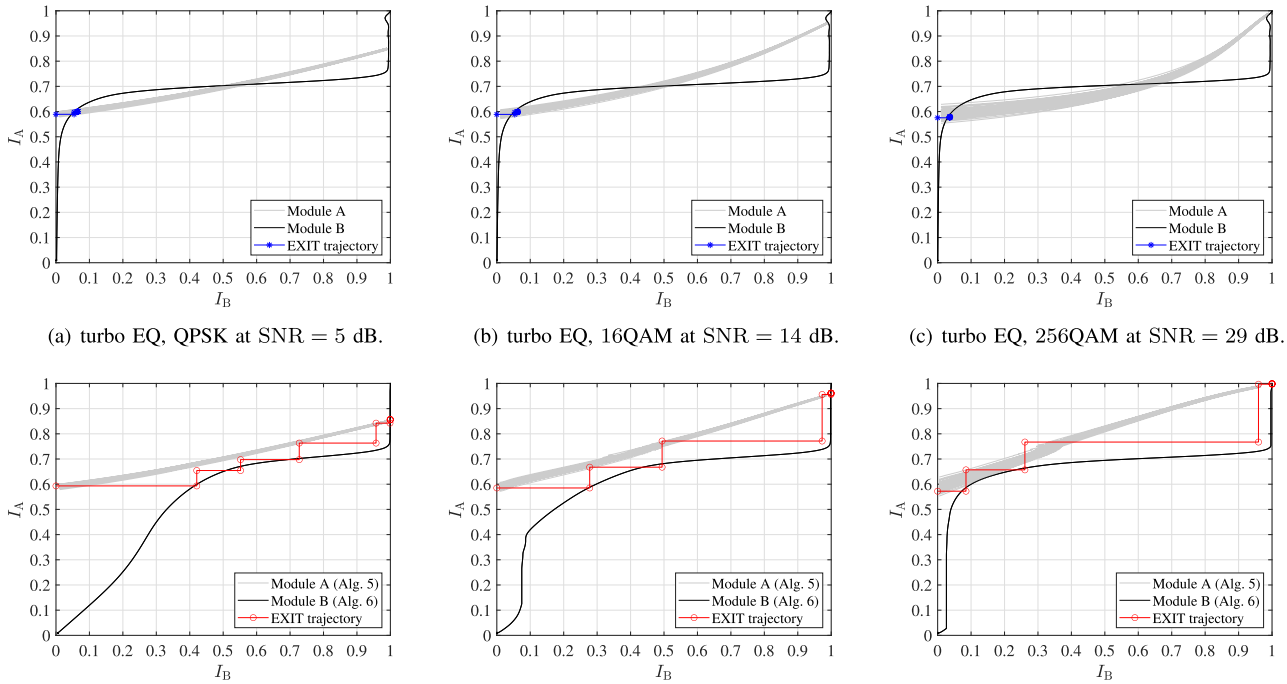

(a) turbo EQ, QPSK at SNR = 5 dB. (b) turbo EQ, 16QAM at SNR = 14 dB. (c) turbo EQ, 256QAM at SNR = 29 dB.

(d) EP-based IDD, QPSK at SNR = 5 dB. (e) EP-based IDD, 16QAM at SNR = 14 dB. (f) EP-based IDD, 256QAM at SNR = 29 dB.

FIGURE 13. EXIT chart analysis for $(N,M) = (32,32)$.

this model, the MIMO channel matrix $\boldsymbol{H}_k$ in (1) can be expressed as

$$\boldsymbol{H}_k = \boldsymbol{R}_{\mathrm{RX}}^{1/2} \boldsymbol{G}_k \boldsymbol{R}_{\mathrm{TX}}^{1/2}, \tag{21}$$

where each element of $\boldsymbol{G}_k \in \mathbb{C}^{N\times M}$ representing the small-scale fading follows $\mathcal{CN}(0,1)$. $\boldsymbol{R}_{\mathrm{RX}} \in \mathbb{R}^{N\times N}$ and $\boldsymbol{R}_{\mathrm{TX}} \in \mathbb{R}^{M\times M}$ denote the spatial correlation matrices on the TX and RX sides, respectively. In the uplink system assumed in this paper, the TX antennas are uncorrelated, *i.e.*, $\boldsymbol{R}_{\mathrm{TX}} = \boldsymbol{I}_M$. Each element of $\boldsymbol{R}_{\mathrm{RX}}$ is generated according to the exponential decay model [67], as

$$\boldsymbol{R}_{\mathrm{RX}} = \begin{cases} 1 & i = j \\ \rho^{|i-j|} & i \neq j \end{cases}, \tag{22}$$

where $\rho \in [0,1]$ denotes the fading correlation coefficient between two distinct RX antennas on the BS side.

B. BER PERFORMANCE

Fig. 14 shows the BER performance as a function of SNR in the large MU-MIMO-OFDM systems, where the correlation coefficient is set to $\rho = 0.6$. The simulation parameters are the same as those listed in Tab. 1 of Section III-G. Since the SC/MMSE detector performs interference suppression via matrix inversion, it is capable of gradually improving detection accuracy through iterative processing, even under correlated MIMO channels. However, beyond the 4th iteration, the SC/MMSE turbo equalization–which generates extrinsic values in the LLR domain–suffers from a significant degradation in iterative gain as the modulation order increases, due to increasing inconsistency with the consistency condition. In contrast, in the case of EP-based IDD, extrinsic values are generated in the symbol domain, enabling appropriate extrinsic value exchange even in correlated MIMO detection. As a result, the impact of self-feedback is effectively mitigated, and high iterative detection gains are successfully maintained.

An interesting insight gained from these results is that, while the overall trends are similar to those observed in uncorrelated MIMO channels, the superiority of EP-based IDD over SC/MMSE turbo equalization becomes even more pronounced. This is because spatial correlation among fading coefficients degrades the signal detection capability of the SC/MMSE detector, leading to increased residual interference and making it difficult to maintain the independence among bit-wise LLRs. Thus, as the detection problem becomes more challenging, EP-based IDD proves to be an increasingly effective detection strategy.

C. EVALUATION VIA EXIT CHART ANALYSIS

Finally, the EXIT chart for the MIMO configurations $(N, M) = (32, 16)$ and $(32, 24)$ with $\rho = 0.6$ are shown in Figs. 15 and 16, respectively. Since the EXIT curves of Module B are plotted under the assumption that interference is ideally suppressed by the SC/MMSE detector and that the output noise can be modeled as uncorrelated AWGN, some mismatch between the EXIT curves of each module and the corresponding EXIT trajectory can be observed compared to the uncorrelated MIMO case. Nevertheless, the overall shape of the EXIT curves reasonably captures the behavior of the EXIT trajectory, and the analysis maintains sufficient accuracy for characterizing the iterative behavior of EP-based

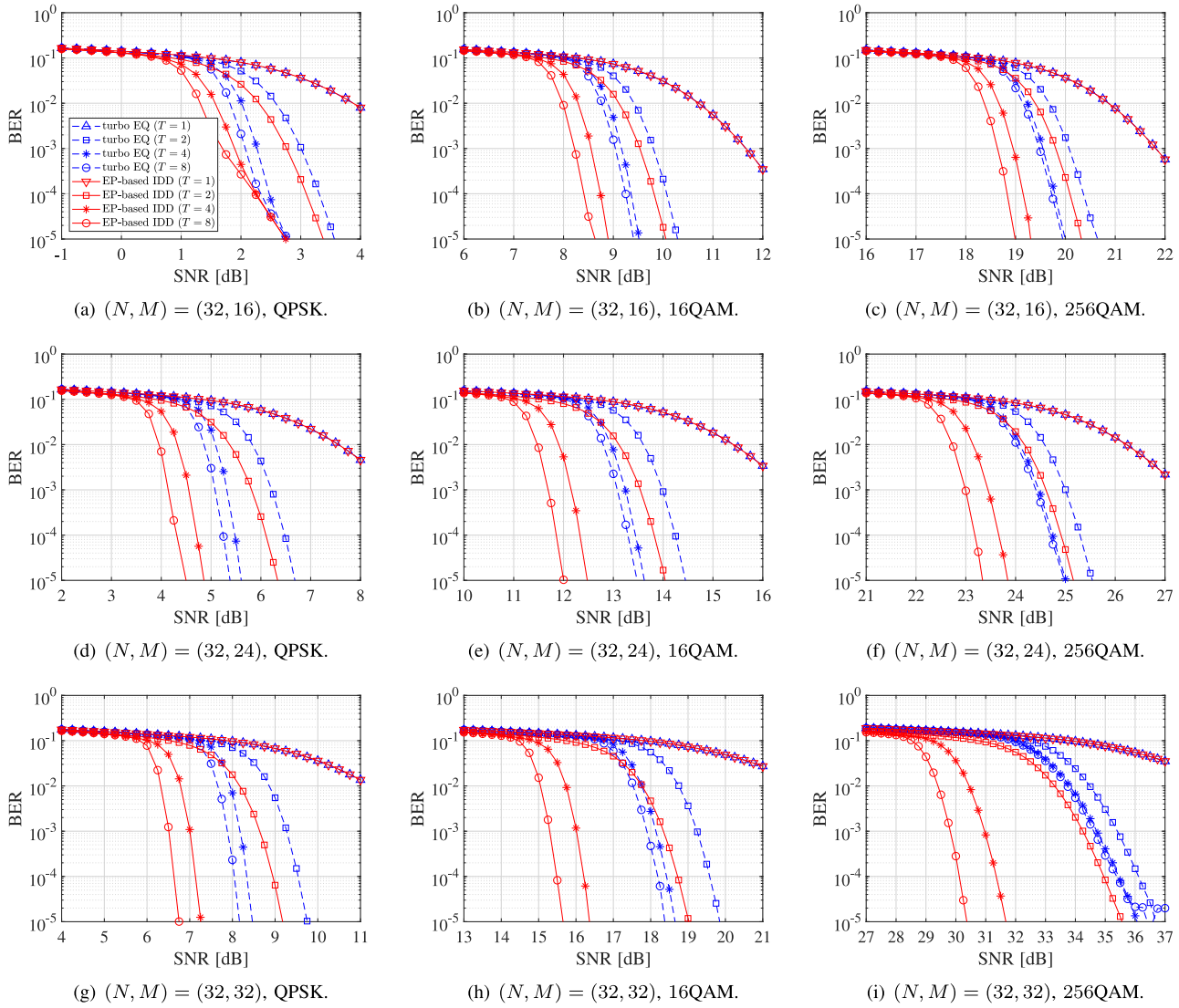

(a) $(N, M) = (32, 16)$, QPSK. (b) $(N, M) = (32, 16)$, 16QAM. (c) $(N, M) = (32, 16)$, 256QAM.

(d) $(N, M) = (32, 24)$, QPSK. (e) $(N, M) = (32, 24)$, 16QAM. (f) $(N, M) = (32, 24)$, 256QAM.

(g) $(N, M) = (32, 32)$, QPSK. (h) $(N, M) = (32, 32)$, 16QAM. (i) $(N, M) = (32, 32)$, 256QAM.

FIGURE 14. BER performance versus SNR for various MIMO configurations with $\rho = 0.6$ and various modulation schemes.

IDD algorithms. These observations confirm the robustness of the proposed framework.

Based on the above investigations, it has been demonstrated that EP-based IDD can achieve significantly robust performance across a wide range of modulation schemes, MIMO configurations, and channel conditions. Moreover, the proposed EXIT chart analysis has been validated as an effective framework for accurately analyzing the iterative behavior of EP-based IDD under practical system sizes.

VI. CONCLUSION

In this paper, we proposed a novel EXIT chart analysis framework to investigate the convergence behavior of EP-based IDD, specifically accommodating the extrinsic value exchange mechanism via MM. Leveraging this framework, we theoretically and numerically compared the extrinsic value exchange mechanisms of SC/MMSE turbo equalization and EP-based IDD, thereby clarifying their fundamental differences. In SC/MMSE turbo equalization, extrinsic value generation is performed in the LLR domain via extrinsic LLRs, whereas in EP-based IDD, it is performed in the symbol domain via MM. The implementation of higher-order modulation schemes complicates the maintenance of the LLR consistency condition in turbo equalization, leading to significant performance degradation. In contrast, EP-based IDD, which considers the discrete constraints of the symbols and matches both the first and second-order moments of the message, demonstrated superior robustness in preserving MUD accuracy. To analyze these observations, we extended the classical EXIT chart analysis to accommodate EP-based IDD. In particular, we appropriately addressed the MI loss that arises during the conversion from bit-wise LLRs to symbol estimates under high-order modulation, and detailed the mathematical derivations necessary for accurately plotting the EXIT curves. Comprehensive numerical simulations were conducted across various conditions, including different modulation schemes, MIMO configurations, and levels of spatial correlation. The results confirmed the robustness and

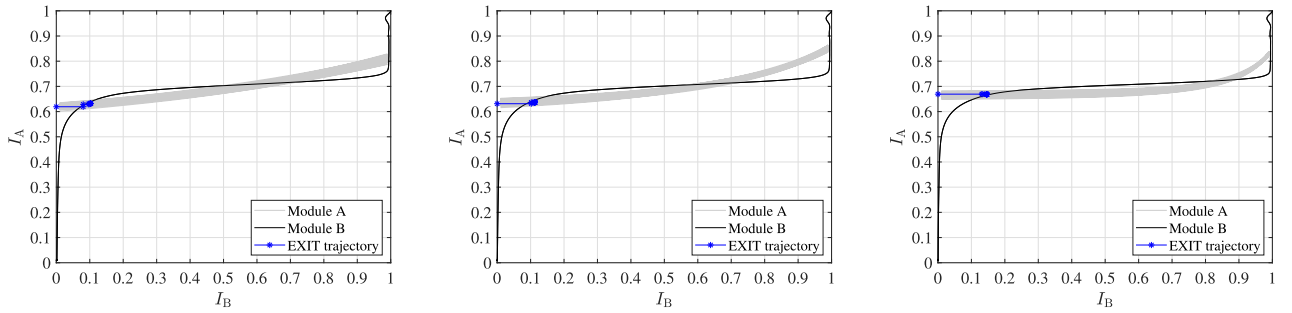

(a) turbo EQ, QPSK, at SNR = 1.5 dB. (b) turbo EQ, 16QAM, at SNR = 8.5 dB. (c) turbo EQ, 256QAM, at SNR = 19 dB.

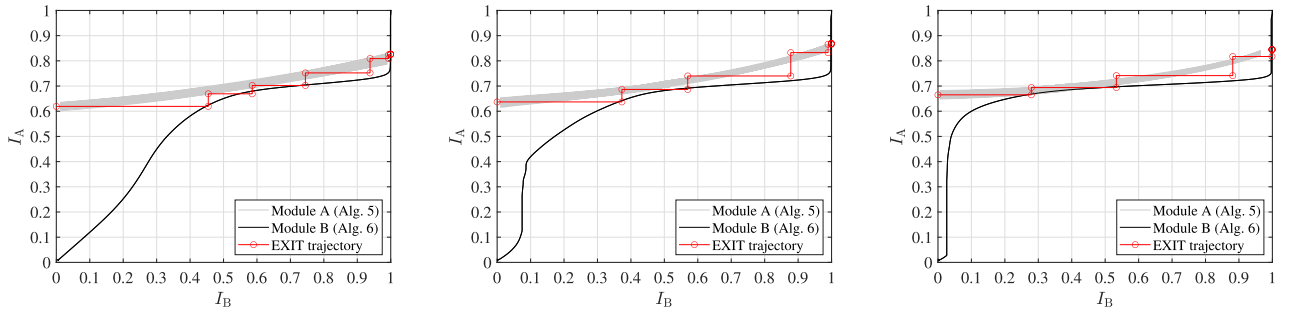

(d) EP-based IDD, QPSK, at SNR = 1.5 dB. (e) EP-based IDD, 16QAM, at SNR = 8.5 dB. (f) EP-based IDD, 256QAM, at SNR = 19 dB.

FIGURE 15. EXIT chart analysis for a correlated channel model with (*N*,*M*) = (32,16).

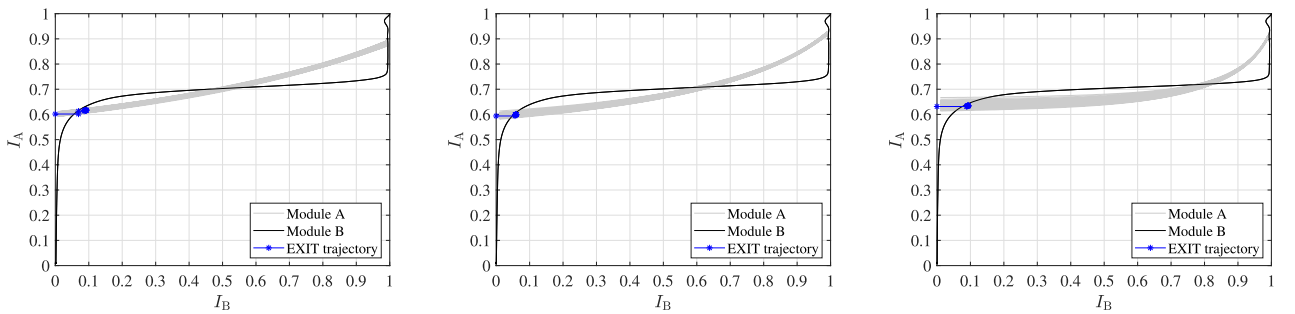

(a) turbo EQ, QPSK, at SNR = 4.5 dB. (b) turbo EQ, 16QAM, at SNR = 12 dB. (c) turbo EQ, 256QAM, at SNR = 23.5 dB.

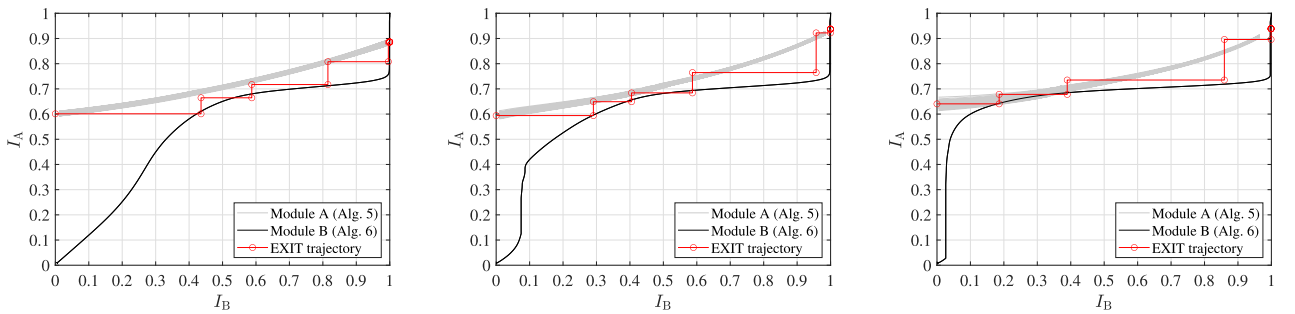

(d) EP-based IDD, QPSK, at SNR = 4.5 dB. (e) EP-based IDD, 16QAM, at SNR = 12 dB. (f) EP-based IDD, 256QAM, at SNR = 23.5 dB.

FIGURE 16. EXIT chart analysis for a correlated channel model with (*N*,*M*) = (32,24).

validity of the proposed framework, offering new insights into the design and analysis of EP-based IDD from a semi-theoretical perspective. Based on all the above results, it has been demonstrated that extrinsic value generation in the symbol domain, which accounts for the discrete constraints of symbols, operates more robustly than extrinsic value generation in the LLR domain, which is highly sensitive to correlations among LLRs.

REFERENCES

[1] M. Vaezi et al., "Cellular, wide-area, and non-terrestrial IoT: A survey on 5G advances and the road toward 6G," *IEEE Commun. Surveys Tuts.*, vol. 24, no. 2, pp. 1117–1174, 2nd Quart., 2022.

[2] W. Saad, M. Bennis, and M. Chen, "A vision of 6G wireless systems: Applications, trends, technologies, and open research problems," *IEEE Netw.*, vol. 34, no. 3, pp. 134–142, May/Jun. 2020.

[3] K. Shafique, B. A. Khawaja, F. Sabir, S. Qazi, and M. Mustaqim, "Internet of Things (IoT) for next-generation smart systems: A review of current challenges, future trends and prospects for emerging 5G-IoT scenarios," *IEEE Access*, vol. 8, pp. 23022–23040, 2020.

[4] L. Chettri and R. Bera, "A comprehensive survey on Internet of Things (IoT) toward 5G wireless systems," *IEEE Internet Things J.*, vol. 7, no. 1, pp. 16–32, Jan. 2020.

[5] G. A. Akpakwu, B. J. Silva, G. P. Hancke, and A. M. Abu-Mahfouz, "A survey on 5G networks for the Internet of Things: Communication technologies and challenges," *IEEE Access*, vol. 6, pp. 3619–3647, 2018.

[6] B. S. Khan, S. Jangsher, A. Ahmed, and A. Al-Dweik, "URLLC and eMBB in 5G industrial IoT: A survey," *IEEE Open J. Commun. Soc.*, vol. 3, pp. 1134–1163, 2022.

[7] D. C. Nguyen et al., "6G Internet of Things: A comprehensive survey," *IEEE Internet Things J.*, vol. 9, no. 1, pp. 359–383, Jan. 2022.

[8] F. Guo, F. R. Yu, H. Zhang, X. Li, H. Ji, and V. C. M. Leung, "Enabling massive IoT toward 6G: A comprehensive survey," *IEEE Internet Things J.*, vol. 8, no. 15, pp. 11891–11915, Aug. 2021.

[9] C.-X. Wang et al., "On the road to 6G: Visions, requirements, key technologies, and testbeds," *IEEE Commun. Surveys Tuts.*, vol. 25, no. 2, pp. 905–974, 2nd Quart., 2023.

[10] H. Tataria, M. Shafi, A. F. Molisch, M. Dohler, H. Sjöland, and F. Tufvesson, "6G wireless systems: Vision, requirements, challenges, insights, and opportunities," *Proc. IEEE*, vol. 109, no. 7, pp. 1166–1199, Jul. 2021.

[11] M. Alsabah et al., "6G wireless communications networks: A comprehensive survey," *IEEE Access*, vol. 9, pp. 148191–148243, 2021.

[12] K. Ito, T. Takahashi, K. Ishibashi, K. Igarashi, and S. Ibi, "Joint channel, CFO, and data estimation via Bayesian inference for multi-user MIMO-OFDM systems," *IEEE Trans. Wireless Commun.*, vol. 24, no. 3, pp. 1898–1915, Mar. 2025.

[13] B. M. Lee and H. Yang, "Massive MIMO for Industrial Internet of Things in cyber-physical systems," *IEEE Trans. Ind. Informat.*, vol. 14, no. 6, pp. 2641–2652, Jun. 2018.

[14] H. Iimori, T. Takahashi, K. Ishibashi, G. T. F. de Abreu, and W. Yu, "Grant-free access via bilinear inference for cell-free MIMO with low-coherence pilots," *IEEE Trans. Wireless Commun.*, vol. 20, no. 11, pp. 7694–7710, Nov. 2021.

[15] T. Takahashi, H. Iimori, K. Ando, K. Ishibashi, S. Ibi, and G. T. F. de Abreu, "Bayesian receiver design via bilinear inference for cell-free massive MIMO with low-resolution ADCs," *IEEE Trans. Wireless Commun.*, vol. 22, no. 7, pp. 4756–4772, Jul. 2023.

[16] K. Ito, T. Takahashi, S. Ibi, and S. Sampei, "Bilinear Gaussian belief propagation for massive MIMO detection with non-orthogonal pilots," *IEEE Trans. Commun.*, vol. 72, no. 2, pp. 1045–1061, Feb. 2024.

[17] S. Yang and L. Hanzo, "Fifty years of MIMO detection: The road to large-scale MIMOs," *IEEE Commun. Surveys Tuts.*, vol. 17, no. 4, pp. 1941–1988, 4th Quart., 2015.

[18] A. Chockalingam and B. S. Rajan, *Large MIMO Systems*. Cambridge, U.K.: Cambridge Univ. Press, 2014.

[19] J.-C. Chen, "A low complexity data detection algorithm for uplink multiuser massive MIMO systems," *IEEE J. Sel. Areas Commun.*, vol. 35, no. 8, pp. 1701–1714, Aug. 2017.

[20] T. Takahashi, S. Ibi, and S. Sampei, "Design of criterion for adaptively scaled belief in iterative large MIMO detection," *IEICE Trans. Commun.*, vol. E102-B, no. 2, pp. 285–297, 2019.

[21] M. Khani, M. Alizadeh, J. Hoydis, and P. Fleming, "Adaptive neural signal detection for massive MIMO," *IEEE Trans. Wireless Commun.*, vol. 19, no. 8, pp. 5635–5648, Aug. 2020.

[22] R. El Chall, F. Nouvel, M. Helard, and M. Liu, "Iterative receivers combining MIMO detection with turbo decoding: Performance-complexity trade-offs," *EURASIP J. Wireless Commun. Netw.*, vol. 2015, no. 1, p. 69, Dec. 2015, doi: 10.1186/s13638-015-0305-6.

[23] W.-C. Sun, W.-H. Wu, C.-H. Yang, and Y.-L. Ueng, "An iterative detection and decoding receiver for LDPC-coded MIMO systems," *IEEE Trans. Circuits Syst. I, Reg. Papers*, vol. 62, no. 10, pp. 2512–2522, Oct. 2015.

[24] H. Omori, T. Asai, and T. Matsumoto, "A matched filter approximation for SC/MMSE iterative equalizers," *IEEE Commun. Lett.*, vol. 5, no. 7, pp. 310–312, Jul. 2001.

[25] M. Tüchler, R. Koetter, and A. Singer, "Turbo equalization: Principles and new results," *IEEE Trans. Commun.*, vol. 50, no. 5, pp. 754–767, May 2002.

[26] K. Kansanen and T. Matsumoto, "An analytical method for MMSE MIMO turbo equalizer EXIT chart computation," *IEEE Trans. Wireless Commun.*, vol. 6, no. 1, pp. 59–63, Jan. 2007.

[27] C. Douillard et al., "Iterative correction of intersymbol interference: Turbo-equalization," *Eur. Trans. Telecommun.*, vol. 6, no. 5, pp. 507–511, 1995.

[28] L. Hanzo, T. H. Liew, B. L. Yeap, R. Y. S. Tee, and S. X. Ng, *Turbo Coding, Turbo Equalisation and Space-Time Coding: EXIT-Chart-Aided Near-Capacity Designs for Wireless Channels*. Hoboken, NJ, USA: Wiley, Mar. 2011.

[29] T. Richardson and R. Urbanke, "The capacity of low-density parity-check codes under message-passing decoding," *IEEE Trans. Inf. Theory*, vol. 47, no. 2, pp. 599–618, Feb. 2001.

[30] J. Hagenauer, "The EXIT chart - introduction to extrinsic information transfer in iterative processing," in *Proc. 12th Eur. Signal Process. Conf.*, 2004, pp. 1541–1548.

[31] M. Tüchler and A. C. Singer, "Turbo equalization: An overview," *IEEE Trans. Inf. Theory*, vol. 57, no. 2, pp. 920–952, Jan. 2011.

[32] R. Tamaki, K. Ito, T. Takahashi, S. Ibi, and S. Sampei, "Suppression of self-noise feedback in GAMP for highly correlated large MIMO detection," in *Proc. Int. Conf. Commun. (ICC)*, 2022, pp. 1300–1305.

[33] T. P. Minka. "Expectation propagation for approximate Bayesian inference." 2013. [Online]. Available: http://arxiv.org/abs/1301.2294

[34] J. Céspedes, P. M. Olmos, M. Sánchez-Fernández, and F. Perez-Cruz, "Expectation propagation detection for high-order high-dimensional MIMO systems," *IEEE Trans. Commun.*, vol. 62, no. 8, pp. 2840–2849, Aug. 2014.

[35] S. Rangan, P. Schniter, and A. K. Fletcher, "Vector approximate message passing," *IEEE Trans. Inf. Theory*, vol. 65, no. 10, pp. 6664–6684, Oct. 2019.

[36] K. Takeuchi, "Rigorous dynamics of expectation-propagation-based signal recovery from unitarily invariant measurements," *IEEE Trans. Inf. Theory*, vol. 66, no. 1, pp. 368–386, May 2020.

[37] I. Santos, J. J. Murillo-Fuentes, and E. Arias-de Reyna, "A double EP-based proposal for turbo Equalization," *IEEE Signal Process. Lett.*, vol. 27, pp. 121–125, 2020.

[38] J. J. Murillo-Fuentes, I. Santos, J. C. Aradillas, and M. Sánchez-Fernández, "A low-complexity double EP-based detector for iterative detection and decoding in MIMO," *IEEE Trans. Commun.*, vol. 69, no. 3, pp. 1538–1547, Mar. 2021.

[39] S. ten Brink, "Convergence behavior of iteratively decoded parallel concatenated codes," *IEEE Trans. Commun.*, vol. 49, no. 10, pp. 1727–1737, Oct. 2001.

[40] A. Ashikhmin, G. Kramer, and S. T. Brink, "Extrinsic information transfer functions: Model and erasure channel properties," *IEEE Trans. Inf. Theory*, vol. 50, no. 11, pp. 2657–2673, Nov. 2004.

[41] E. Sharon, A. Ashikhmin, and S. Litsyn, "Analysis of low-density parity-check codes based on EXIT functions," *IEEE Trans. Commun.*, vol. 54, no. 8, pp. 1407–1414, Aug. 2006.

[42] S. Ibi, T. Matsumoto, R. Thomä, S. Sampei, and N. Morinaga, "EXIT chart-aided adaptive coding for multilevel BICM with turbo Equalization in frequency-selective MIMO channels," *IEEE Trans. Veh. Technol.*, vol. 56, no. 6, pp. 3757–3769, Nov. 2007.

[43] M. El-Hajjar and L. Hanzo, "EXIT charts for system design and analysis," *IEEE Commun. Surveys Tuts.*, vol. 16, no. 1, pp. 127–153, 1st Quart., 2014.

[44] Z. B. K. Egilmez, L. Xiang, R. G. Maunder, and L. Hanzo, "A soft-input soft-output polar decoding algorithm for turbo-detection in MIMO-aided 5G new radio," *IEEE Trans. Veh. Technol.*, vol. 71, no. 6, pp. 6454–6468, Jun. 2022.

[45] R. Wohlgenannt, K. Kansanen, D. Tujkovic, and T. Matsumoto, "Outage-based LDPC code design for SC/MMSE turbo-equalization," in *Proc. IEEE Veh. Technol. Conf. (VTC)*, vol. 1, 2005, pp. 505–509.

[46] H. Obata, S. Ibi, and S. Sampei, "A design for an EXIT chart based scheduling and rate control for multi-user MIMO systems," *IEEE Trans. Wireless Commun.*, vol. 8, no. 10, pp. 5124–5132, Oct. 2009.

[47] M. A. Ahmed and C. C. Tsimenidis, "Tight upper bound performance of full-duplex MIMO-BICM-IDD systems in the presence of residual self-interference," *IEEE Trans. Wireless Commun.*, vol. 17, no. 1, pp. 520–532, Jan. 2018.

[48] T. Kobayashi, T. Takahashi, S. Ibi, and S. Sampei, "Concatenated structure of EP and turbo Equalizer for overloaded massive MIMO detection," in *Proc. 21st IEEE Annu. Comsum. Commun. Netw. Conf. (CCNC)*, 2024, pp. 690–695.

[49] S. Yang, T. Lv, R. G. Maunder, and L. Hanzo, "From nominal to true a posteriori probabilities: An exact Bayesian theorem based probabilistic data association approach for iterative MIMO detection and decoding," *IEEE Trans. Commun.*, vol. 61, no. 7, pp. 2782–2793, Jul. 2013.

[50] T. Takahashi, A. Tölli, S. Ibi, and S. Sampei, "Low-complexity large MIMO detection via layered belief propagation in beam domain," *IEEE Trans. Wireless Commun.*, vol. 21, no. 1, pp. 234–249, Jan. 2022.

[51] M. Grossmann and T. Matsumoto, "Nonlinear frequency domain MMSE turbo equalization using probabilistic data association," *IEEE Commun. Lett.*, vol. 12, no. 4, pp. 295–297, Apr. 2008.

[52] J. Ma, L. Liu, X. Yuan, and L. Ping, "On orthogonal AMP in coded linear vector systems," *IEEE Trans. Wireless Commun.*, vol. 18, no. 12, pp. 5658–5672, Dec. 2019.

[53] J. Ma and L. Ping, "Orthogonal AMP," *IEEE Access*, vol. 5, pp. 2020–2033, 2017.

[54] D. L. Donoho, A. Maleki, and A. Montanari, "Message-passing algorithms for compressed sensing," *Proc. Nat. Acad. Sci. USA*, vol. 106, no. 45, pp. 18914–18919, 2009.

[55] M. Bayati and A. Montanari, "The dynamics of message passing on dense graphs, with applications to compressed sensing," *IEEE Trans. Inf. Theory*, vol. 57, no. 2, pp. 764–785, Feb. 2011.

[56] M. Bayati, M. Lelarge, and A. Montanari, "Universality in polytope phase transitions and message passing algorithms," *Ann. Appl. Probab.*, vol. 25, no. 2, pp. 753–822, Apr. 2015. [Online]. Available: http://dx.doi.org/10.1214/14-AAP1010

[57] T. Takahashi, S. Ibi, and S. Sampei, "Design of adaptively scaled belief in multi-dimensional signal detection for higher-order modulation," *IEEE Trans. Commun.*, vol. 67, no. 3, pp. 1986–2001, Mar. 2019.

[58] D. Shirase, T. Takahashi, S. Ibi, K. Muraoka, N. Ishii, and S. Sampei, "Deep unfolding-aided gaussian belief propagation for correlated large MIMO detection," in *Proc. IEEE GLOBECOM*, 2020, pp. 1–6.

[59] D. Shirase, T. Takahashi, S. Ibi, K. Muraoka, N. Ishii, and S. Sampei, "Negentropy-aware loss function for trainable belief propagation in coded MIMO detection," in *Proc. IEEE GLOBECOM*, 2021, pp. 1–6.

[60] T. Furudoi, T. Takahashi, S. Ibi, and H. Ochiai. "Discrete-valued signal estimation via low-complexity message passing algorithm for highly correlated measurements." 2024. [Online]. Available: https://arxiv.org/abs/2411.07558

[61] Y. Liu, Y. Shen, W. Zhou, X. Tan, X. You, and C. Zhang, "Iterative EP detection and decoding of polar-coded MIMO systems," *IEEE Commun. Lett.*, vol. 27, no. 4, pp. 1075–1079, Apr. 2023.

[62] X. Tan et al., "Expectation propagation-based parallel iterative detection and decoding for massive MIMO," *IEEE Trans. Veh. Technol.*, vol. 73, no. 1, pp. 93–106, Jan. 2024.

[63] X. Wang and H. Poor, "Iterative (turbo) soft interference cancellation and decoding for coded CDMA," *IEEE Trans. Commun.*, vol. 47, no. 7, pp. 1046–1061, Jul. 1999.

[64] K. Takeda, K. Ishihara, and F. Adachi, "Frequency-domain ICI cancellation with MMSE equalization for DS-CDMA downlink," *IEICE Trans. Commun.*, vol. 89-B, pp. 3335–3343, Dec. 2006.

[65] *IEEE Standard for Information Technology—Telecommunications and Information Exchange Between Systems Local and Metropolitan Area Networks—Specific Requirements—Part 11: Wireless LAN Medium Access Control (MAC) and Physical Layer (PHY) Specifications*, IEEE Standard 802.11-2016, 2016.

[66] H. V. Poor and S. Verdu, "Probability of error in MMSE multiuser detection," *IEEE Trans. Inf. Theory*, vol. 43, no. 3, pp. 858–871, May 1997.

[67] M. Chiani, M. Win, and A. Zanella, "On the capacity of spatially correlated MIMO Rayleigh-fading channels," *IEEE Trans. Inf. Theory*, vol. 49, no. 10, pp. 2363–2371, Oct. 2003.

FUGA KOBAYASHI (Graduate Student Member, IEEE) received the B.E. degree in communication engineering from The University of Osaka, Osaka, Japan, in 2024, where he is currently pursuing the M.E. degree with the Graduate School of Engineering. His research interests include wireless communications, Bayesian inference, and signal processing.

TAKUMI TAKAHASHI (Member, IEEE) received the B.E., M.E., and Ph.D. degrees in communication engineering from The University of Osaka, Osaka, Japan, in 2016, 2017, and 2019, respectively. From 2018 to 2019, he was a Visiting Researcher with the Centre for Wireless Communications, University of Oulu, Finland. In 2019, he joined the Graduate School of Engineering, The University of Osaka, as an Assistant Professor, where he is currently an Associate Professor. His current research interests include Bayesian inference, belief propagation, signal processing, and wireless communications. He received the 80th Best Paper Award from IEICE and the 2019 and 2023 Best Paper Awards from IEICE Communication Society, and the 40th Telecom System Technology Awards from the Telecommunication Advancement Foundation. He was certified as an Exemplary Reviewer of IEEE WIRELESS COMMUNICATIONS LETTERS in 2023.

SHINSUKE IBI (Senior Member, IEEE) received the B.E. degree in advanced engineering from Suzuka College of Technology, Japan, in 2002, and the M.E. and Ph.D. degrees in communication engineering from The University of Osaka, Japan, in 2004 and 2006, respectively. From 2005 to 2006, he was a Visiting Researcher with the Centre for Wireless Communications, University of Oulu, Finland. In 2006, he joined the Graduate School of Engineering, University of Osaka. From 2010 to 2011, he was a Visiting Researcher with the University of Southampton, U.K. In 2019, he moved to Doshisha University, and he is currently a Professor with the Faculty of Science and Engineering. His research interests include EXIT-based coding theory, iterative detection, digital signal processing, cognitive radio, and communication theory. He received the 64th, 71st, and 80th Best Paper Awards from IEICE, 2017, 2018, 2019, and 2023 Best Paper Awards from IEICE Communication Society, and the 24th and 40th Telecom System Technology Awards from the Telecommunication Advancement Foundation.

HIDEKI OCHIAI (Fellow, IEEE) received the B.E. degree in communication engineering from Osaka University, Osaka, Japan, in 1996, and the M.E. and Ph.D. degrees in information and communication engineering from The University of Tokyo, Tokyo, Japan, in 1998 and 2001, respectively. From 1994 to 1995, he was with the Department of Electrical Engineering, University of California at Los Angeles, Los Angeles, CA, USA, under the scholarship of the Ministry of Education, Science and Culture. From 2001 to 2003, he was a Research Associate with The University of Electro-Communications, Tokyo. From 2003 to 2024, he was with Yokohama National University, Yokohama, Japan, where he has been a Professor since 2015. Since 2024, he has been a Professor with The University of Osaka, Osaka, Japan. From 2003 to 2004, he was a Visiting Scientist with Harvard University, Cambridge, MA, USA. From 2019 to 2020, he was a Visiting Professor with the University of Waterloo, Waterloo, ON, Canada, and a Visiting Fellow with Princeton University, Princeton, NJ, USA. His research focuses on the areas of wireless communications and networks. He was an Editor of IEEE TRANSACTIONS ON WIRELESS COMMUNICATIONS from 2007 to 2011 and IEEE WIRELESS COMMUNICATIONS LETTERS from 2011 to 2016.